

INFORMATION TO USERS

This manuscript has been reproduced from the microfilm master. UMI films the text directly from the original or copy submitted. Thus, some thesis and dissertation copies are in typewriter face, while others may be from any type of computer printer.

The quality of this reproduction is dependent upon the quality of the copy submitted. Broken or indistinct print, colored or poor quality illustrations and photographs, print bleedthrough, substandard margins, and improper alignment can adversely affect reproduction.

In the unlikely event that the author did not send UMI a complete manuscript and there are missing pages, these will be noted. Also, if unauthorized copyright material had to be removed, a note will indicate the deletion.

Oversize materials (e.g., maps, drawings, charts) are reproduced by sectioning the original, beginning at the upper left-hand corner and continuing from left to right in equal sections with small overlaps.

**ProQuest Information and Learning
300 North Zeeb Road, Ann Arbor, MI 48106-1346 USA
800-521-0600**

UMI[®]

University of Alberta

**Study of Interactions between Micron-Sized Poly(styrene-co-butyl
acrylate) Particles at a Sub-Glassy Temperature**

by

Michael Hudec



A thesis submitted to the Faculty of Graduate Studies and Research in partial
fulfillment of the requirements for the degree of
Master of Science

in

Chemical Engineering

Department of Chemical and Materials Engineering

Edmonton, Alberta
Spring 2005



Library and
Archives Canada

Bibliothèque et
Archives Canada

0-494-08083-3

Published Heritage
Branch

Direction du
Patrimoine de l'édition

395 Wellington Street
Ottawa ON K1A 0N4
Canada

395, rue Wellington
Ottawa ON K1A 0N4
Canada

Your file *Votre référence*
ISBN:
Our file *Notre référence*
ISBN:

NOTICE:

The author has granted a non-exclusive license allowing Library and Archives Canada to reproduce, publish, archive, preserve, conserve, communicate to the public by telecommunication or on the Internet, loan, distribute and sell theses worldwide, for commercial or non-commercial purposes, in microform, paper, electronic and/or any other formats.

The author retains copyright ownership and moral rights in this thesis. Neither the thesis nor substantial extracts from it may be printed or otherwise reproduced without the author's permission.

AVIS:

L'auteur a accordé une licence non exclusive permettant à la Bibliothèque et Archives Canada de reproduire, publier, archiver, sauvegarder, conserver, transmettre au public par télécommunication ou par l'Internet, prêter, distribuer et vendre des thèses partout dans le monde, à des fins commerciales ou autres, sur support microforme, papier, électronique et/ou autres formats.

L'auteur conserve la propriété du droit d'auteur et des droits moraux qui protègent cette thèse. Ni la thèse ni des extraits substantiels de celle-ci ne doivent être imprimés ou autrement reproduits sans son autorisation.

In compliance with the Canadian Privacy Act some supporting forms may have been removed from this thesis.

Conformément à la loi canadienne sur la protection de la vie privée, quelques formulaires secondaires ont été enlevés de cette thèse.

While these forms may be included in the document page count, their removal does not represent any loss of content from the thesis.

Bien que ces formulaires aient inclus dans la pagination, il n'y aura aucun contenu manquant.

Canada

Abstract

In coatings applications, solvent-based systems are often undesirable due to the negative impact of volatile organic compounds on the environment. This has led to major incentives to shift to water-based systems, which involve aqueous dispersions of colloidal latex particles. Along with the push to expand the use of water-based systems, there is also a need to understand the basic science behind the film formation process. For this, novel micromechanical techniques were developed in this study with the focus of evaluating their potential for studying film formation. (70:30 wt%) poly(styrene-co-butyl acrylate) particles, stabilized with poly(vinyl alcohol), were used to demonstrate these new techniques. The particles were studied below their glass transition temperature to prevent viscous behaviour, thus simplifying experiments for this initial investigation. The young's modulus of individual particles was quantified (10MPa). As well, capillary attraction from water evaporation was found to be the only force able to cause particle-particle adhesion.

Acknowledgements

For their expertise in chemical engineering and conducting research, and for their constant support, I would like to thank my supervisors Tony Yeung and Phillip Choi. They have both been wonderful to work with and have provided advices that I will benefit from for years to come.

Many thanks goes to Alberta Ingenuity for financial support.

I am sincerely grateful to Professor Huining Xiao and his group in the Chemical Engineering Department at the University of New Brunswick. Their synthesis of poly (styrene-co-butyl acrylate) particles in a timely fashion allowed the project to proceed smoothly.

Finally, I would like to thank my wife and family who were a source of encouragement and love throughout the time spent on this project.

Contents

1. Introduction.....	1-5
2. Literature Review	6-25
2.1 Dry Sintering (Dillon et al.)	6
2.2 Elastic Spheres Subjected to Capillary Forces (Brown)	7
2.3 Rupture of Stabilizing Layers (Vanderhoff et al.).....	10
2.4 Coalescence Driven by Osmotic Stress (Sheetz)	10
2.5 Further Confirmation of Dry Sintering using DSC (Mahr).....	13
2.6 Refinement of Brown's Theory (Mason)	14
2.7 Viscoelastic Spheres Subjected to Capillary Forces (Lamprecht)	15
2.8 JKR Theory to Characterize Coalescence (Kendall and Padgett)	16
2.9 Insufficiency of Capillary Force Models (Eckersley and Rudin).....	18
2.10 Further Confirmation of Sheetz's Theory (Dobler et al.).....	19
2.11 The Plasticizing Role of Water on Latex Particles (Sperry et al.)	20
2.12 ESEM and MAIE Film Formation Observations (Keddie et al.).....	21
2.13 Wet and Dry Film Formation Study with AFM (Lin and Meier)	22
2.14 A Macroscopic Mechanical Model (Routh and Russel)	23
3. Present Approach: A Novel Micromechanical Study.....	26-29
4. Materials and Methods.....	30-47
4.1 Microtool Manufacturing	30
4.2 Synthesis of Latex Particles	34
4.3 Glass Transition Temperature of Latex Particles	36
4.4 Microscope Setup.....	37
4.5 Isolating Individual Particles.....	38
4.6 Tendency for Particle-Particle Adhesion	40
4.7 Elasticity of Individual Latex Particles	40
4.8 The Contact/Adhesion Experiment	43
4.9 Simulating Water Evaporation	45
5. Results and Discussion.....	48-61
5.1 Tendency for Particle-Particle Adhesion	48
5.2 Elasticity of Individual Latex Particles	49
5.3 The Contact/Adhesion Experiment	53
5.4 Simulating Water Evaporation	56
5.5 Mechanism of Particle-Particle Adhesion.....	59
5.6 Future Work	60
6. Conclusions.....	62-63
Bibliography.....	64-65

Appendix A	66-72
Appendix B	73-79

Tables

Table 1: Dimensionless Parameters and their Physical Meanings.....	25
Table 2: Trial 1 of Hertz Contact Experiment in Air (Particle Radius of 15 μm)	73
Table 3: Trial 2 of Hertz Contact Experiment in Air..... (Particle Radius of 10 μm)	73
Table 4: Trial 1 of Hertz Contact Experiment in Water (Particle Radius of 10 μm)	73
Table 5: Trial 2 of Hertz Contact Experiment in Water (Particle Radius of 10 μm)	74
Table 6: Trials for Contact/Adhesion Experiment (Particle Radii of 10 μm)	79
Table 7: Trials for Adhesion Due to Capillary Attraction (Particle Radii of 10 μm)	79

Figures

Figure 1: Dispersed vs. Dissolved Film Formation	2
Figure 2: Attractive and Repulsive Forces in Particle Coalescence	4
Figure 3: (a) Close Packing of Particles	7
(b) Sintering of Two Particles	
Figure 4: (a) Hemi-Spherical Capillary Between Top Layer Particles.....	9
(b) Top Layer Particles Viewed From Above Used to Relate R to r	
Figure 5: Water Evaporation Between Two Particles with Stabilizing Layer.....	10
Figure 6: Capillary with Air/Water to Polymer/Water Contact Angle.....	11
Figure 7: (a) Cross Sectional Area of a Particle in its Deformed State	14
(b) Direction of Force Between Top Particle and Three Particles Below	
(c) Geometry to Calculate Modified Capillary Pressure	
Figure 8: Two Polymer Particles with Contact Radius a and Energy Loss ξ	17
Figure 9: Corrugation Height ch Measured with AFM	22
Figure 10: (a) Straight Micropipette	28
(b) Microcantilever	
(c) Deflected Microcantilever	
Figure 11: Micropipette with Closed End.....	30
Figure 12: Pipette Puller Setup	31
Figure 13: Truncated Micropipette	32
Figure 14: Pipette Truncating Setup	32
Figure 15: Setup for Bending Micropipettes into Microcantilevers.....	34
Figure 16: Setup for Bending Micropipettes into Microcantilevers	34
as seen under Microscope	
Figure 17: (70:30) Poly (styrene-co-butyl acrylate) Latex Dispersion Stabilized with Poly (vinyl – alcohol) as viewed under an optical microscope	36
Figure 18: Microscope Experimental Setup	38

Figure 19: Particle on the End of a Microtool	39
Figure 20: Solid Spherical Body Deformed due to an Applied Force.....	41
Figure 21: (a) A Microcantilever with a Glass Bead on its End.....	43
(b) Particle and Glass Bead Cantilever in the Hertz Experiment	
Figure 22: Two Particles Forced Together with Microtools in Contact/Adhesion Experiment.....	45
Figure 23: Possible Natural Forces Responsible for Film Formation.....	46
Figure 24: Water Bridge between Particles	47
Figure 25: (a) (70:30) Poly (styrene-co-butyl acrylate) Dispersion.....	48
(b) Partially Coalesced (70:30) Poly (styrene-co-butyl acrylate) Particles	
Figure 26: Trial 1 of Particle Deformation vs Contact Force on log-log plot	51
in Air (Particle Radius of 15 μ m)	
Figure 27: Trial 1 of Particle Deformation vs Contact Force on log-log plot	51
in Water (Particle Radius of 10 μ m)	
Figure 28: Approximate Relationship Between Particle Adhesion Force.....	54
and Contact Force	
Figure 29: (a) Individual Beams of Cantilever	66
(b) Forces on Cantilever	
Figure 30: Output Graphs Characterizing Cantilever Spring Constant	72
Figure 31: Trial 1 of Particle Deformation vs Contact Force on log-log plot	75
in Air (Particle Radius of 15 μ m)	
Figure 32: Trial 1 of Particle Deformation vs Contact Force	75
in Air (Particle Radius of 15 μ m)	
Figure 33: Trial 2 of Particle Deformation vs Contact Force on log-log plot	76
in Air (Particle Radius of 10 μ m)	
Figure 34: Trial 2 of Particle Deformation vs Contact Force	76
in Air (Particle Radius of 10 μ m)	
Figure 35: Trial 1 of Particle Deformation vs Contact Force on log-log plot	77
in Water (Particle Radius of 10 μ m)	

Figure 36: Trial 1 of Particle Deformation vs Contact Force	77
in Water (Particle Radius of 10μm)	
Figure 37: Trial 2 of Particle Deformation vs Contact Force on log-log plot	78
in Water (Particle Radius of 10μm)	
Figure 38: Trial 2 of Particle Deformation vs Contact Force	78
in Water (Particle Radius of 10μm)	

Symbols, Nomenclature, and Abbreviations

θ : Coalescence Angle

γ : Interfacial Tension

η : Polymer Viscosity

R : Particle Radius

t : Time

P_C : Capillary Pressure

$\gamma_{w/a}$: Water/Air Interfacial Tension

R : Radius of Hemispherical Capillary

P_G : Average Elastic Stress

G : Particle Shear Modulus

ν : Poisson's Ratio

h : Particle Axial Deformation

a : Contact Radius of Curvature

ϕ : Air/Water/Polymer Contact Angle

$\Delta\xi$: Change in Surface Energy

ΔA : Change in Surface Area

$\gamma_{a/p}$: Air/Polymer Interfacial Tension

F_C : Capillary Force

F_G : Elastic Deformation Force

f : Deformation Factor

$a(t)$: Time Dependent Contact Radius

$J(t)$: Polymer Creep Compliance

$F(t)$: Time Dependant Contact Force

F : Contact Force

ν_i : Poisson Ratio of Particle i

E_i : Elastic Modulus of Particle i

R_i : Radius of Particle i

ζ : Energy Release when Two Surfaces of Unit Area move into Proximity

G^* : Particle Complex Shear Modulus

T_g : Glass Transition Temperature

DSC : Differential Scanning Calorimetry

MFFT : Minimum Film Formation Temperature

ESEM : Environmental Scanning Electron Microscopy

MAIE : Multi-Angle Incidence Ellipsometry

AFM : Atomic Force Microscopy

ch : Corrugation Height

\dot{E} : Evaporation Rate

H : Initial Film Thickness

ϕ_m : Volume Fraction of Film

N : Average Number of Nearest Neighbors

ε : Macroscopic Strain

σ_t : Macroscopic Stress

G_∞ : Particle High Frequency Modulus

η_o : Particle Low Shear Viscosity

η_∞ : Particle High Frequency Viscosity

KT : Thermal Energy

η_w : Water Viscosity

k : Cantilever Spring Constant

x : Horizontal Cantilever Deflection

C : Proportionality Constant in Hertz Theory

R' : Radius of Glass Bead in Hertz Experiment

F_h : Horizontal Force on Cantilever

F_v : Vertical Reaction Force on Cantilever

L_i : Length of Cantilever Beam i

x_i : Distance along Cantilever Beam i

z_i : Deflection of Cantilever Beam i

M_i : Moment along Cantilever Beam i

I_i : Moment of Inertia along Cantilever Beam i

E_g : Young's Modulus of Glass

r_{in} : Inner Radius of Cantilever Pipette

r_{out} : Outer Radius of Cantilever Pipette

dv : Vertical Deflection of Cantilever

dh : Horizontal Deflection of Cantilever

y_{1i} : Variable 1 used in Numeric Calculation of Spring Constant for Beam i

y_{2i} : Variable 2 used in Numeric Calculation of Spring Constant for Beam i

1. Introduction

Surface properties of materials are often important for engineering applications.

In many instances, it is beneficial for a material's surface to be modified so that it will interact with its surroundings in a favourable way, either for protection or for reactivity. Applying a polymeric coating to a material surface is one way to make such a modification. Although there are multiple ways to create a polymer coating, a common and efficient way is to coat a solid substrate with a liquid carrier that contains polymer, whereby a polymer residue/film is left behind on the surface when the liquid phase evaporates.

There are two ways in which film-forming polymers can be put into a liquid carrier. One way is to dissolve the polymer using an organic solvent, while another way is to disperse it as very small particles in water; the latter system is known as *water-borne coatings*. (The polymer is assumed, as is true in most applications, to be insoluble in water but soluble in certain organic solvents.) The distinction between the two approaches is shown in Figure 1. Although both methods will lead to the formation of a thin film, there is a trade-off in choosing between the two options. A dissolved polymer solution produces a better quality film than when dispersed, but has very negative effects on the environment due to the release of volatile organic compounds (VOCs). As such, there has been increased needs to understand and to improve on the film formation mechanism in water-borne coatings so that they can be more widely used. Water-borne coatings are at present useful for such products as paints, adhesives, caulks and sealants, paper coatings, textiles, and carpets.¹ They could possibly be developed for more

applications, where higher quality films are required, if a more thorough understanding of the underlying mechanisms of film formation is achieved.

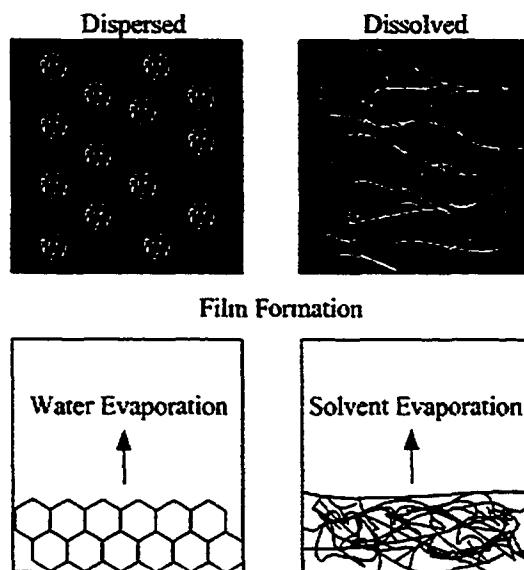


Figure 1: Dispersed vs. dissolved film formation²

In water-borne coatings, dispersed polymer systems — often referred to as “latex dispersions” — are created using a method known as emulsion polymerization. This polymerization technique creates colloidal sized particles in water, with diameters between 50nm -1 μ m. The process by which these very small polymer particles are transformed into a continuous film is called *coalescence*.³ As evident from the discrepancies in the literature, coalescence is a very complicated and often ill-defined phenomenon. Indeed, despite over 50 years of research, conclusive evidence on what causes coalescence of the dispersed particles is still lacking.^{1, 4-17} At present, it is believed that the film formation process can be divided into three steps:^{1-2, 18}

1. Initial water evaporation increases the concentration of particles and brings them into close contact.

2. Particles are forced together causing them to deform and adhere to produce a structure without voids.
3. Diffusion of polymer chains across particle boundaries yields a continuous film with mechanical integrity.

In the end, it is believed that the original particles are no longer distinguishable.

Research has been conducted on all three of these stages of film formation, but the one that has received the most attention — and being the most controversial — is the particle compaction or deformation step (step two).¹ Opinion is divided as to the exact forces which are responsible for pushing the particles together to produce the structure without voids.¹⁶ Figure 2 shows the forces that could be responsible for causing coalescence. It also shows those forces that could be responsible for *preventing* coalescence because they are just as important in understanding the second stage of film formation. From theory of the interactions between microscopic particles (colloidal theory), we would predict that six types of forces could be involved in the coalescing process:

1. When two contacting particles are in suspension, it is thermodynamically favorable to minimize the total surface area of the particles — a coalescence process driven by the interfacial tension between the polymer material and the surrounding water. This is sometimes called a “wet sintering” process.
2. After the surrounding water has completely evaporated, it is thermodynamically favorable to minimize the total surface area of two contacting particles — a coalescence process driven by the surface tension of the polymer material (i.e., the interfacial tension between the polymer material and air). This is sometimes called a “dry sintering” process.
3. A water bridge between two polymer particles could draw the particles together through the action of the air/water surface tension (the capillary effect).
4. van der Waals forces would lead to an attraction between identical spheres.

5. Elastic deformation forces would resist coalescence by striving to retain the particles' original shapes.
6. Colloidal stabilizing forces could prevent coalescence through electrostatic or steric repulsion at the particle surfaces.

The relative roles played by these different forces have not yet been ascertained and attempts to explain coalescence in terms of these forces have led to many different theories of film formation. Additional forces may also be possible. An example of an additional attraction force is described by Sheetz¹ in his diffusion theory which will be described in chapter 2. Whether any other forces play significant roles remains an open question.

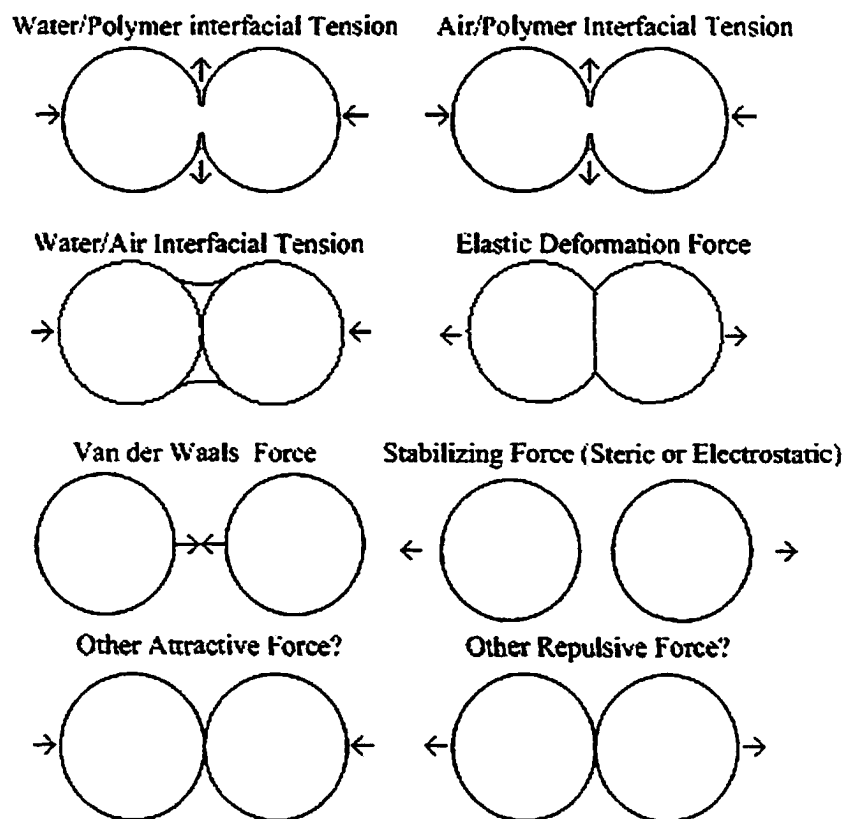


Figure 2: Attractive and repulsive forces in particle coalescence

If we could understand the forces that cause the particles to come together and lose their individuality, we would be in a better position to predict the optimum method for generating thin films using latex dispersions. The focus of

this present research is to evaluate new micromechanical techniques designed to shed light on the forces responsible for causing coalescence in latex dispersions. These techniques involve manipulating *two* individual particles with special microtools and studying their ability to adhere to one another in different environments. By observing how *two* particles respond to one another in controlled conditions, we can potentially develop a greater understanding of the mechanisms responsible for film formation. In this work, a case study is presented using (70:30 wt%) poly (styrene-co-butyl acrylate) particles stabilized with poly(vinyl alcohol). These particles are somewhat larger than those in typical latex dispersions, making them observable under a light microscope and easily manipulated with special microtools. How these specific particles respond to one another in different environments is determined. Also, physical properties of the particles such as elastic modulus are quantified for greater understanding of their nature. These particles are studied at room temperature, which is well below the temperature at which they would normally form a film. Higher temperature studies are reserved for a time when the techniques presented here have been refined. The procedures outlined in this work will pave the way for further studies into film formation using such a micromechanical approach.

2. Literature Review

Past research into the second stage of film formation (i.e., the particle deformation step) will be summarized according to workers who have made significant contributions to the field. The following is a discussion of selected publications that yield information about the experiments and theories that have been developed and give an indication of where the field is at present. The main goal in all past research was to develop a clearer fundamental understanding of the second stage of film formation through experiment and theoretical models.

2.1 Dry Sintering (Dillon *et al.* ⁴)

Dillon *et al.* assumed that polymer particles in a latex dispersion are Newtonian liquids and that water evaporates completely from the system before coalescence, bringing the particles into contact with one another as shown in figure 3a. They decided to experimentally test a theory developed by Frenkel ¹⁹ for the sintering of two liquid drops, which assumes that the coalescence process is driven by air/polymer interfacial tension. This model predicts the time dependence of the coalescence angle θ , shown in figure 3b, given the interfacial tension γ between the particles and surrounding medium, the polymer viscosity η , the particle radius R , and the particle-particle contact time t . Assuming low Reynolds number flow, Frenkel derived the following relation:

$$\theta^2 = \frac{3\gamma t}{2\pi\eta R} \quad (1)$$

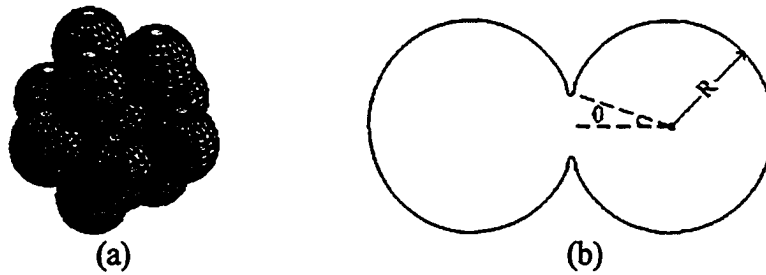


Figure 3: (a) Close packing of particles. (b) Sintering of two particles.

To experimentally verify the validity of using Frenkel's theory, Dillon *et al.* let a latex dispersion dry at room temperature and observed the film with an electron microscope. Using the particle size distribution, they quantified the relationship between θ and R and compared it with Frenkel's theory. They obtained average θ values for particles of the same radii and plotted θ^2 vs $1/R$, obtaining a linear relationship as predicted by the model. In addition, η was varied with the addition of a plasticizer. Using the same procedure as for the radius, they obtained a linear relationship between θ^2 and $1/\eta$, as predicted by equation (1). These results, which support Frenkel's theory, suggest that the coalescence process is driven by air/polymer interfacial tension.

2.2 Elastic Spheres Subjected to Capillary Forces (Brown ⁵)

Brown pointed out that polymer particles are not ideal Newtonian liquids and contented that water evaporation should play a role in film formation. His belief is based on the observations that film formation is complete only when water is completely evaporated, and that the rate of water evaporation seems to play a role in determining whether a film will form. Within the framework of his particle coalescence model, brown developed a criterion for film formation. He pointed out that there are attractive and repulsive forces between particles and, as long as

attraction outweighs repulsion, coalescence will occur. He believes that capillary forces from water evaporation are the most important attractive forces and that the elasticity of the particles, which resists deformation, provides the dominant repulsion. Therefore, if capillary forces are greater than elastic repulsion, film formation will occur.

In Brown's analysis, the top three spheres in figure 3a, which are situated in the top layer of the film, are half immersed in water prior to the second step in film formation. The resulting void between them is assumed to contain a hemispherical meniscus (i.e., half a water drop) as shown in figure 4a. Since the meniscus is assumed to be hemi-spherical, the pressure difference P_C between the water and the air, and also the top and bottom half of the top layer particles, is given by the Young-Laplace equation:

$$P_C = \frac{2\gamma_{w/a}}{r} \quad (2)$$

where $\gamma_{w/a}$ is the interfacial tension between water and air, and r is the radius of the hemi-spherical meniscus. Brown believes that this capillary stress P_C is responsible for providing a downward force on the top layer of polymer particles, which in turn causes coalescence of the layers below. This effect is believed to continue as the water level descends down through the particle layers. Through simple geometry (Figure 4b), Brown obtains a new and final relation for P_C that depends on particle radius R :

$$P_C = 2(2\sqrt{3} + 3) \frac{\gamma_{w/a}}{R} \approx 12.9 \frac{\gamma_{w/a}}{R} \quad (3)$$

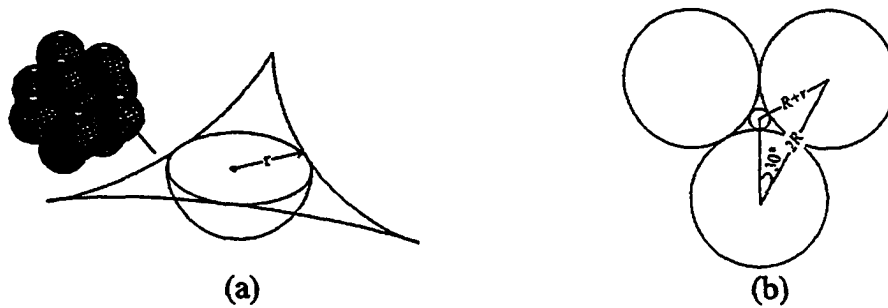


Figure 4: (a) Hemi-spherical capillary between top layer particles. (b) Top layer particles viewed from above used to relate R to r .

Using primarily results of Hertz theory for elastic deformation²⁰, Brown derived an average elastic stress P_G pushing back against capillary stress:

$$P_G = \frac{8G}{3\pi(1-\nu)} \sqrt{\frac{2h}{R}} \quad (4)$$

where G is the particle shear modulus, ν is the Poisson's ratio (which is approximately $\frac{1}{2}$ for incompressible elastomers), and h is the particle axial deformation.

Brown states that the maximum axial deformation is $h=0.095R$, which occurs when the particles become hexagons due to deformation from six nearest neighbors, giving rise to a maximum for P_G of:

$$P_G \approx 0.37G \quad (5)$$

Assuming that the capillary and elastic deformation pressures act over the same area, Brown compared the two pressures and obtained his quantitative criterion for film formation — that the capillary pressure must be larger than the elastic deformation pressure for film formation to occur:

$$G < \frac{35\gamma_{w/a}}{R} \quad (6)$$

2.3 Rupture of Stabilizing Layers (Vanderhoff *et al.* ⁶)

Vanderhoff *et al.* considered the coalescence of two spherical particles of radius R , each with stabilizing layer of thickness s which resists coalescence ($s/R \ll 1$). Between the two particles, there is initially a liquid bridge, as shown in figure 5, which eventually evaporates. Vanderhoff *et al.* proposed that the water/air interfacial tension during evaporation causes a large attraction which ruptures the stabilizing layer. Once this occurs, the interiors of the particles, which behave as a viscous liquids, come into contact. Vanderhoff and coworkers suggested that, once in contact, wet sintering due to water/polymer interfacial tension acts in tandem with water/air interfacial tension to drive the coalescence process until all water is evaporated. They supported their theory by numerically calculating the attractive pressures between the particles as a function of the degree of coalescence, demonstrating that large pressures are possible when water/polymer interfacial tension and water/air interfacial tension act in tandem.

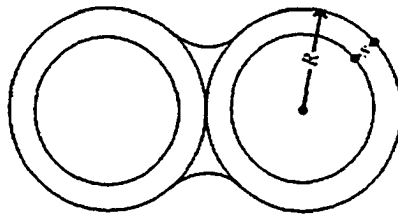


Figure 5: Water evaporation between two particles with stabilizing layers.

2.4 Coalescence Driven by Osmotic Stresses (Sheetz ⁷)

Sheetz conducted three experiments from which he developed his theory on film formation.

In his first experiment, Sheetz provided evidence that water/polymer interfacial tension influences coalescence. He dried latex dispersions well below their glass

transition temperature and then studied the solid content of these dried latexes before and after immersion in a hot water bath. Solids content is a measure of the existence of particle voids where trace water can reside after filtration of bulk water. Percent solids content is given by:

$$\% \text{solid} = \frac{\text{mass of dry solid}}{(\text{mass of dry solid} + \text{mass of excess water in particle voids})} \quad (7)$$

Sheetz noticed that immersion in the hot water bath increases solids content and therefore coalescence. However, he found that the solids content did not reach 100%, indicating that water/polymer interfacial tension can only partially drive coalescence.

Sheetz's second and third experiments provided evidence for a new theory that he developed involving diffusion of water through a closed surface layer. Sheetz built his new theory upon the assumption that capillary forces, similar in nature to those in Brown's model⁵, act to force top layer particles laterally together in addition to forcing them down onto layers below. Sheetz proposed the theory based on the assumption of the existence of a contact angle ϕ between the air/water and polymer/water interfaces as shown in figure 6. In using hemispherical menisci, Brown assumed this contact angle ϕ to be zero.

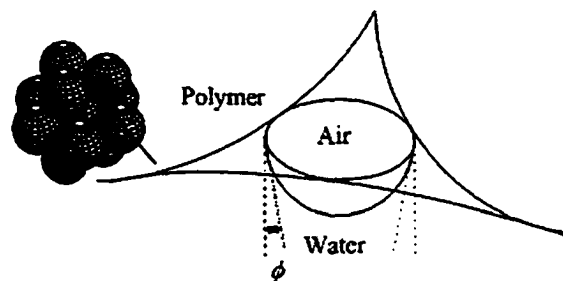


Figure 6: Capillary with air/water to polymer/water contact angle

Sheetz stated that if ϕ is large enough, the top layer of particles will push laterally together and coalesce to create a closed surface layer. With the presence of a surface layer, Sheetz commented on the need for an alternate route for water evaporation. He suggested that continued water evaporation occurs by diffusion through polymer particles in the closed top layer and that this diffusion provides an osmotic compressive force to coalesce the particles. Sheetz described his diffusion theory by considering a cylindrical vessel filled with a latex dispersion and covered with a frictionless piston that is permeable to water vapour only. When the vessel is placed in a low humidity environment, water evaporates and osmotic pressure pushes the piston down, compressing particles within the water together.

Sheetz performed two experiments to support his diffusion theory. In the first experiment, he dried two dispersions with polymers of different water permeabilities at the same time and determined the solids content of each as they dried. At the beginning, the two samples dried at comparable rates. However, at some point, Sheetz observed that the sample with the higher permeability to water “broke away” and dried at a much faster rate, indicating the effect of diffusion through the polymer surface. In the second experiment, a latex was deposited on a substrate. One part of it was covered with a membrane permeable to water vapour, while the other part was not. After drying, the part that was covered was clear, while the other part was cloudy. A clear film indicates less particle voids for light to scatter and therefore more coalescence. This indicated that the latex covered with a permeable membrane let water diffuse through the membrane,

creating a larger compressive force, resulting in a better film. Sheetz concluded that capillary effects and wet sintering are important in the first stages of the particle coalescence process, but in the subsequent stages, diffusion through the particle surface layer causes a large compressive force which results in film formation.

2.5 Further Confirmation of Dry Sintering using DSC (Mahr ⁸)

Mahr designed an experiment to test if polymer particles are able to coalesce without water, driven only by the polymer/air interfacial tension. He examined the coalescence of dry particles by measuring the disappearance of their surface area. The loss of surface area is directly related to a loss of surface energy, which Mahr measured using differential scanning calorimetry (DSC). The change in surface energy, $\Delta\xi$, is given by:

$$\Delta\xi = \gamma_{a/p}\Delta A \quad (8)$$

where $\gamma_{a/p}$ is the air/polymer interfacial tension, and ΔA is the change in surface area. Mahr's experiment involved freeze drying a dispersion to bring the particles into contact. Once frozen, the particles were locked in position and Mahr assumed that the particles were uncoalesced. Mahr then carried out DSC measurements twice on the particles. In the first run, the particles coalesced, giving rise to a heat loss as shown through DSC. In the second run, however, there was no coalescence. Instead, the second run exhibited reversible effects of heating and cooling. Mahr then found the difference between the DSC curves produced in the two runs and thus singled out an irreversible coalescence curve.

The resulting curve implies the amount of energy lost through coalescence and thus the loss of surface area. Since the particles were dry and showed evidence of coalescence, Mahr concluded that coalescence may proceed in the absence of water and therefore in the absence of water/air interfacial tension from water evaporation.

2.6 Refinement of Brown's Theory (Mason⁹)

Mason's contribution to the understanding of film formation is a modification of Brown's theory⁵. Brown assumed that the capillary and elastic stresses, P_C and P_G , act over equal areas. Mason showed that the areas over which these stresses act are not the same: The capillary stress P_C acts over the cross sectional area of a top layer particle in figure 3a, causing the particle to be forced down evenly onto three particles beneath it, while the elastic deformation stress P_G acts over the area of contact between a set of two particles as they deform.

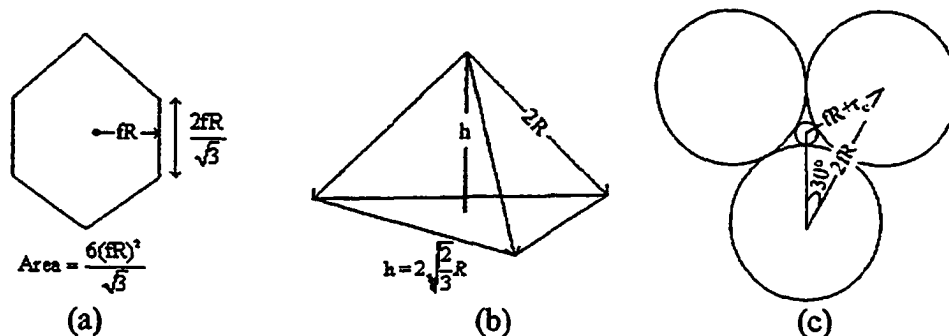


Figure 7: (a) Cross sectional area of a particle in its deformed state. (b) Direction of forces between top particle and three particles below. (c) Geometry to calculate modified capillary pressure.

Mason assumed that particles are hexagonally close packed and eventually are deformed by their twelve nearest neighbors to become 12-faced dodecahedrons. Through geometry considerations, Mason derived an expression for capillary

force F_C , which is the force between a top layer particle and each of the three particles it contacts beneath it. His expression for the capillary force is:

$$F_C = \frac{P_C(\text{x-section area of top particle})}{(3 \text{ particles})(\text{component in each particles direction})} = \frac{\left(\frac{2\gamma_{w/a}}{\sqrt{3}} - 1\right)R \left(\frac{6}{\sqrt{3}} f^2 R^2\right)}{(3)\left(\sqrt{\frac{2}{3}}\right)} \quad (9)$$

where the cross sectional area of a top layer particle is that of a hexagon as shown in figure 7a (i.e., a circle deformed by a factor f from six nearest neighbors), the capillary pressure P_C is similar to Brown's, but takes the particle deformation factor f into consideration as shown in figure 7c, and the component of force between the top particle and each of the three particles it contacts beneath it is calculated using figure 7b.

Using Brown's definition for the deformation force, but replacing the maximum deflection with $(1-f)R$, Mason arrived at an expression for elastic deformation force F_G :

$$F_G = \frac{16}{3} \sqrt{2} G R^2 (1-f)^{3/2} \quad (10)$$

Placing F_G and F_C into the inequality $F_C > F_G$, and giving f a maximum deformation value of 0.94 (consistent with dodecahedrons), Mason yielded a new condition for film formation:

$$G < 266 \frac{\gamma_{w/a}}{R} \quad (11)$$

2.7 Viscoelastic Spheres Subjected to Capillary Forces (Lamprecht¹⁰)

Lamprecht refined Mason's model⁹ by assuming the polymer material to be viscoelastic instead of elastic. He uses Yang's contact theory²¹ for the contact

radius $a(t)$ between two spheres of radius R forced together with force $F(t)$ and having creep compliance $J(t)$:

$$a^3(t) = \frac{3R}{16} \int_{-\infty}^t J(t-\tau) \frac{dF(\tau)}{d\tau} d\tau \quad (12)$$

Lamprecht obtained the result of this integral by noticing that for $t < 0$, $F(t) = 0$, and for $t \geq 0$, $F(t) = F_c$, a constant from Mason's model. The result is

$$a^3(t) = \frac{3}{16} RJ(t)F_c \quad (13)$$

By substituting Mason's value for capillary force, and noting that contact radius after drying should be greater than or equal to the dodecahedron contact radius $a^3 = 0.0835R^3$, Lamprecht arrived at a new criterion for film formation:

$$\frac{1}{J(\text{drying time})} \leq 95 \frac{\gamma_{a/w}}{R} \quad (14)$$

2.8 Use of JKR Theory to Characterize Coalescence (Kendall and Padgett¹¹)

Kendall and Padgett used the JKR (Johnson, Kendall and Roberts)²² theory to characterize the coalescence of polymer particles. The JKR theory describes equilibrium between two elastic spheres meeting under elastic and surface forces.

It is an extension of Hertz's theory which considers only elastic forces. The JKR theory provides an expression for contact radius a :

$$a^3 = \frac{3}{8} \left(\frac{1-\nu_1^2}{E_1} - \frac{1-\nu_2^2}{E_2} \right) \frac{2R_1R_2}{(R_1+R_2)} \left[F + \frac{3\pi\zeta}{2} \frac{2R_1R_2}{(R_1+R_2)} + \left\{ 3\pi\zeta F \frac{2R_1R_2}{(R_1+R_2)} + \left(\frac{3\pi\zeta}{2} \frac{2R_1R_2}{(R_1+R_2)} \right)^2 \right\}^{\frac{1}{2}} \right] \quad (15)$$

where ν_1 and ν_2 are the Poisson ratios of the respective particles, E_1 and E_2 are the particle elastic moduli, R_1 and R_2 are particle radii, F is an external force pushing

the particles together, and ζ is defined as the energy released when two surfaces of unit area move into proximity. The value of ζ depends on the surface properties of the particles.

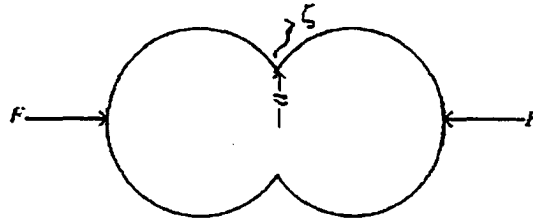


Figure 8: Two polymer particles with contact radius a and energy loss ζ .

Kendall and Padgett believed that the film formation process involves capillary forces due to water evaporation pushing the particles together until the repulsive surface forces in a stable emulsion are overcome and are replaced by an attractive force which pulls the particles together as characterized by the JKR equation.

Kendall and Padgett experimentally showed that the JKR equation applies to particle coalescence in film formation. They first studied macroscopic interactions between two polymer surfaces to determine the interfacial energy ζ and the elastic modulus E of their polymer. They then inserted this information into the JKR equation to predict the contact radius of microscopic polymer particles in film formation. The force F is equated to zero because it is due to capillary attraction and is assumed to vanish when water is gone and the stabilizing layer is ruptured. Observations of contacts under an electron microscope after film formation appear to confirm Kendall and Padgett's model.

2.9 Insufficiency of Capillary Forces (Eckersley and Rudin ¹²)

Eckersley and Rudin presented experimental evidence which demonstrates the insufficiency of the capillary models proposed by Brown⁵, Mason⁹, and Lamprecht¹⁰. Brown, Mason, and Lamprecht claimed that they could predict the occurrence of film formation using only the particle radii R and the shear modulus G of the particles in a latex dispersion. To test their models, Eckersley and Rudin experimentally determined the minimum film formation temperature vs. particle radius for a particular type of dispersed polymer and also determined the complex modulus vs. temperature for the same polymer. They used a long metal bar with a temperature gradient along its length for minimum film formation temperature measurements (i.e., they determined the temperature at which an emulsion dries to form a clear film, indicating no voids to scatter light). For the complex modulus measurements, they used a dynamic mechanical measurement system. From their complex modulus vs. temperature and minimum film formation temperature vs. particle radius profiles, Eckersley and Rudin extracted the temperature for which a particular particle radius forms a film and used this temperature to predict the complex modulus that allowed such film formation to occur. They showed that the complex modulus for a given particle radius can actually be much higher than predicted by the models of Brown, Mason, and Lamprecht. This implies, according to Eckersley and Rudin, that since the capillary force models are insufficient to predict film formation for such high modulus values, other forces in addition to capillary forces must be acting to cause film formation. Eckersley and Rudin therefore support the idea of the existence of surface forces such as

water/polymer interfacial tension acting in tandem with capillary forces to cause film formation.

2.10 Further Confirmation of Sheetz's Theory (Dobler *et al.*¹³)

Dobler *et al.* studied film formation by analysing the effects of particle surface composition on the drying behaviour of films. They modified surface compositions by incorporating different amounts of stabilizing agents to the surfaces of particles. Dobler *et al.* dried many samples with different surface modifications over a range of temperatures and humidities and noted the temperatures and humidities at which coalescence did not occur (i.e., the film is not transparent after drying). From this, they create temperature/humidity limit diagrams for each surface composition and also determine drying kinetics by continuously weighing the samples to calculate the solids content as a function of time.

From their experiments, Dobler *et al.* found no significant difference in the limiting conditions or drying kinetics between dispersions with different particle surface compositions. From this, they concluded that polymer/water surface tension and capillary forces, which depend on the polymer/water/air contact angle and thus particle surface properties, are not involved in film formation. The only phenomenon known to be relatively independent of particle surface properties is Sheetz's diffusion theory.⁷ Dobler *et al.* found evidence backing up Sheetz's theory by observing iridescent spots at the surface of drying dispersions which grew in size until the whole surface was iridescent. This

iridescence indicates, according to Dobler *et al.*, that particles organize regularly at the surface. Dobler *et al.* concluded that film formation occurs by the mechanism described by Sheetz where actual coalescence takes place under very similar circumstances for all types of polymer latexes.

2.11 The Plasticizing Role of Water on Latex Particles (Sperry *et al.* ¹⁴)

Sperry *et al.* studied the effect that water has on film formation by using a temperature gradient bar, similar to that used by Eckersley and Rudin¹², to obtain minimum film formation temperatures (MFFT) (i.e., cloudy to clear transition temperatures) for both wet and pre-dried films. Pre-dried films were dried well below their glass transition temperatures and the particles were assumed uncoalesced, while wet films were normal undried latex dispersions. Sperry *et al.* believed that if water evaporation does have a special force enhancing effect on film formation, then the wet latexes would have significantly lower MFFT values than pre-dried latices. In addition, this special enhancing effect would not be due to plasticization of the polymer particles. To confirm this, they studied both hydrophobic and hydrophilic polymers. Sperry *et al.* found for hydrophobic polymers, which generally do not plasticize in water, that the MFFT values were nearly coincidental in both the wet and dry conditions, but for hydrophilic polymers, the MFFT values in wet conditions were significantly lower. These results indicated, that the only role of water in film formation is that of plasticizing hydrophilic polymer particles. As a result of their findings, Sperry *et al.* considered water evaporation and particle compaction as separate processes —

where the slower of the two is the rate limiting process. Like Kendall and Padget¹¹, Sperry *et al.* invoked the JKR contact theory to describe the forces which serve to induce particle deformation in a drying film.

2.12 Real-Time Observations of Film Formation with ESEM and MAIE (Keddie *et al.*¹⁶)

Keddie *et al.* used two experimental techniques in tandem: Environmental Scanning Electron Microscopy (ESEM) and Multi-Angle-Incidence Ellipsometry (MAIE), to study microstructure and optical characteristics of latexes during the stages of film formation. ESEM is used as it allows real time observation of the samples, while MAIE is useful in following the evolution of latex films by yielding light scattering information. Light scattering is indicative of inter-particle voids and thus the degree of film formation. Keddie *et al.* used four different latex particles with varying glass transition temperatures (i.e., different viscoelastic properties). With each of the latexes, they watched film formation under the ESEM and measured the amount of light scattering with MAIE as the film formation proceeded. They noticed a sharp decrease in the amount of light scattering at a specific time in the film formation process, regardless of glass transition temperature. This indicates that the onset of film formation occurs at nearly the same time in the film formation process, regardless of the intrinsic viscoelastic properties of the polymer. They attributed this abruptness to the evaporation of water (i.e., water/air interfacial tension) in conjunction with particle deformation, which is confirmed by water loss observations and reduced voids under the ESEM. Unlike the sudden start of film formation, however, they

found that continued film formation and loss of particle identity is very much dependent on particle viscoelastic properties. Keddie *et al.* continually observed under the ESEM and found that softer particles lose their identity much faster than harder particles (Harder particles can take up to two weeks to lose their identity or not at all if the glass transition temperature is very low). They attributed continued film formation, after the loss of water, to the reduction of the polymer/air surface area (driven by the corresponding interfacial tension).

2.13 Wet and Dry Film Formation Conditions Studied with AFM (Lin and Meier¹⁷)

Lin and Meier used atomic force microscopy (AFM) to measure the corrugation height ch , as shown in figure 9, as a function of time, to study the kinetics of film formation under wet and dry conditions.

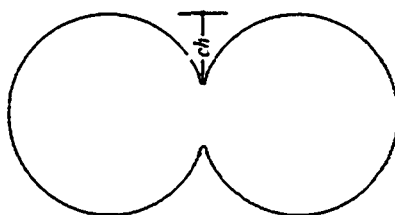


Figure 9: Corrugation height ch measured with AFM

They casted a thin layer of emulsion on multiple substrates, allowing the latexes to dry well below the glass transition temperature of the polymer particles so that the particles pack together but were assumed uncoalesced. In order to partially hydrate the particles, Lin and Meir then placed some of their samples in a very humid environment, allowing water to condense in the interstitial voids of the latex. They then placed all samples in an oven. At select intervals of time, one wet and one dry sample were removed and scanned with the AFM to obtain the

corrugation height of dry and wet latices as functions of time. AFM data revealed that film formation occurs much faster for the wet system; this may have been due to the effect of water/air interfacial tension, water/polymer interfacial tension or plasticization. However, Lin and Meir indicated that plasticization is not an issue with the polymer used, and since the water/polymer interfacial tension is known to be even less than the polymer/air interfacial tension, they concluded that the enhanced film formation must be due to the water/air interfacial tension (i.e., capillary forces from water evaporation in interstitial spaces).

2.14 A Macroscopic Mechanical Model (Routh and Russel¹)

Routh and Russel have constructed an all encompassing model that predicts the system properties for which each of the film formation mechanisms (i.e., water/polymer, air/polymer, water/air interfacial tensions, etc.) plays a role in film formation. This model is based on the belief that each mechanism may be dominant in film formation if given the right system conditions. They created this model using an extension of Frenkel's model for the microscopic interaction between two particles. They used a statistical approach to average the effect of the microscopic interactions over the entire volume of the film, creating a macroscopic stress-strain relationship. Using this approach, they were able to obtain a differential equation describing the macroscopic stress-strain relationship of the film based on dimensionless parameters:

$$\frac{d\bar{\sigma}_t}{dt} + \bar{G}\bar{\sigma}_t + \frac{7\bar{\gamma}}{5} \left(\frac{d\varepsilon}{dt} + \bar{G}\varepsilon \right) = \frac{\bar{\lambda}}{\bar{\eta}} \frac{d}{dt} \left(\varepsilon \frac{d\varepsilon}{dt} \right) + \bar{G}\bar{\lambda}\varepsilon \frac{d\varepsilon}{dt} \quad (16)$$

where the dimensionless parameters and their physical meanings are given in table 1.

Typically, characteristic evaporation timing \bar{t} , macroscopic stresses $\bar{\sigma}_i$ and macroscopic strains ε occur for particular film formation mechanisms. For example, for water/polymer interfacial tension, the stress at the top surface is approximately zero and strain occurs before water evaporation. With these constraints, Routh and Russel found the magnitudes of dimensionless parameters \bar{G} , $\bar{\eta}$, and $\bar{\lambda}$ for water/polymer interfacial tension occurrence (i.e. a 3D surface graph). They used this same procedure for all different mechanisms such as air/polymer interfacial tension and water/air interfacial tension, noting different \bar{t} , $\bar{\sigma}_i$, and ε values for each and obtaining specific theoretical \bar{G} , $\bar{\eta}$, and $\bar{\lambda}$ values in each case. By understanding which dimensionless parameter values (i.e., system properties) cause a particular film formation mechanism, Routh and Russel were able to predict the mechanism that will dominate in a given condition. By predicting results of past experiments, Routh and Russel find their model to be accurate.

To describe the surface film phenomenon predicted by Sheetz, they also develop a dimensionless parameter Pe , which if greater than one, a surface layer would form. This would be due to the particles not being given enough time to distribute themselves in the water before the water evaporates, causing a build up of particles at the surface which would fuse together if particles are sufficiently soft.

Dimensionless Parameters	Physical Meaning
$\bar{t} = \frac{t\dot{E}}{H}$ $t = \text{time}, \dot{E} = \text{Evaporation Rate}, H = \text{Initial Film Thickness}$	scaled time
$\bar{\sigma}_t = \frac{28\sigma_t R}{3N\phi_m\gamma_{w/a}}$ $\phi_m = \text{volume fraction of film},$ $N = \text{average \# of particle nearest neighbors}$	$\frac{\text{stress at top surface}}{\text{capillary pressure}}$
$\bar{\gamma} = \frac{\gamma}{\gamma_{w/a}}$	$\frac{\text{surface tension}}{\text{water-air surface tension}}$
$\bar{G} = \frac{G_{\infty}H}{\dot{E}\eta_o}$ $G_{\infty} = \text{High frequency modulus}, \eta_o = \text{low shear viscosity}$	$\frac{\text{evaporation time}}{\text{polymer relaxation time}}$
$\bar{\lambda} = \frac{\eta_o R\dot{E}}{\gamma_{w/a}H}$	$\frac{\text{time for viscous collapse}}{\text{evaporation time}}$
$\bar{\eta} = \frac{\eta_o}{\eta_{\infty}}$ $\eta_{\infty} = \text{High frequency viscosity}$	$\frac{\text{low shear viscosity}}{\text{high frequency viscosity}}$
$Pe = \frac{6\pi\mu R H \dot{E}}{KT}$ $KT = \text{thermal energy}, \eta_w = \text{water viscosity}$	$\frac{\text{rate of evaporation}}{\text{rate of diffusion}}$

Table 1: Dimensionless parameters and their physical meanings

3. Present Approach: A Novel Micromechanical Study

From the review of past research, it is evident that there are many theories — sometimes mutually contradicting — which describe particle coalescence in the second step of film formation. For each theory, there exists experimental results in the literature which support the proposed mechanism. If all theories are indeed valid, as the experimental results suggest, then the importance of each theory to film formation needs to be ascertained. We propose, similar to Routh and Russel, that particle coalescence is likely a phenomenon which is dependent on many system parameters (i.e., polymer material, polymer surface properties, temperature, etc.) where different theories become valid to describe film formation when the right system parameters are present. To define more precisely how different system parameters affect the forces that drive film formation, more direct experimental work is required. What has been lacking up until now is the ability to perform small scale experiments on the polymer particles themselves. By performing experiments directly on the particles, we can determine how they behave in response to different system parameters.

In this study, we propose a new approach which involves controlled experiments on the simplest unit of film formation — two individual polymer particles. By understanding the interactions of two particles, we can gain insight into the collective behaviour of a film forming system. In order to experiment on individual particles, it is convenient to make them with slightly larger sizes. Particles in industrial latex dispersions, created by emulsion polymerization, are typically very small (less than one micron) and are not visible under an optical

microscope. This makes them very difficult to study individually. However, particles that are somewhat larger (several microns), created using suspension polymerization, can be easily observed with an optical microscope. With the use of special microtools, these larger particles can be manipulated and deformed in controlled experiments. Performing controlled experiments on these somewhat larger particles using microtools is the basis of the present new technique. With these larger particles, trends may be established that will reflect the behaviour of the smaller-sized latex particles found in industrial applications.

The special tools used for studying micron-sized polymer particles are made from glass pipettes whose tips are tapered down to micrometres in size. They are called micropipettes and have found their original usage in the area of biology and biophysics (study of biological cells).²³ These micropipettes are hollow and use suction pressures to grab onto the cells. In this study, polymer particles are similarly manipulated. A picture of a micropipette is shown in figure 10a. Three-axis micromanipulators control the motions of the micropipettes. In addition to a straight pipette, another microtool called the microcantilever is used as a force transducer. Figure 10b shows a picture of such a cantilever. The microcantilever's advantage lies in its ability to detect very weak forces (as small as nanonewtons). Because of its shape, it acts like a spring when deflected horizontally. Figure 10c shows a deflected cantilever. Using beam theory, the effective stiffness of a microcantilever can be evaluated based on its geometry. Once the stiffness k is found, it can be used to evaluate minute forces which cause cantilever deflection. The deflection x is easily measured from analysis of

microscopic images; the deflection force F is simply the product of the cantilever stiffness and its deflection (i.e., $F = kx$).

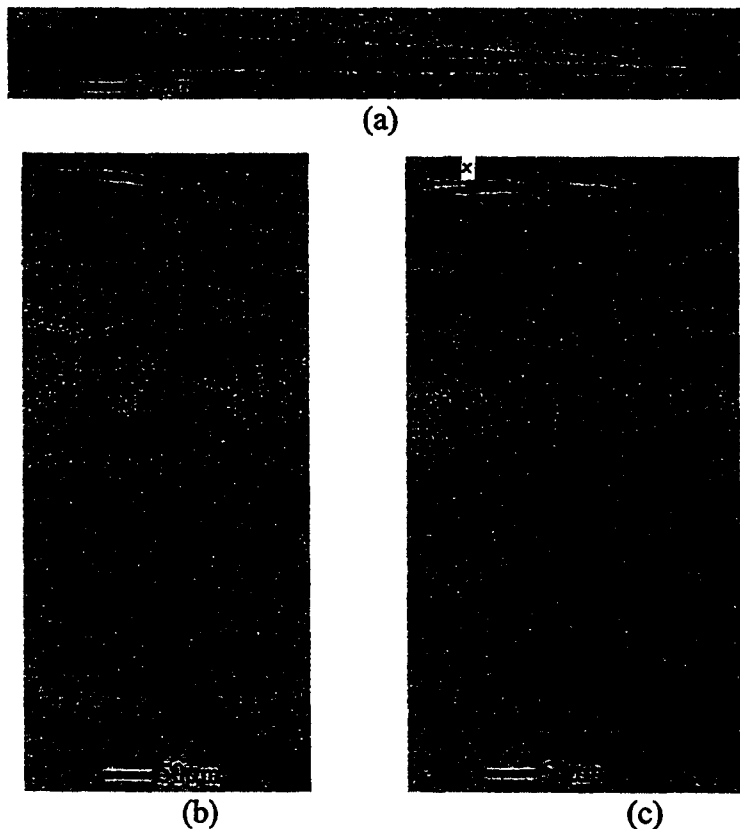


Figure 10: (a) Straight micropipette (b) microcantilever (c) deflected microcantilever

The straight micropipette and the microcantilever, shown in figures 10a and 10c, are used together. With particles on the ends of these two microtools, controlled force-based experiments can be performed in simulated film formation environments to determine which forces are important in the coalescence of two polymer particles.

In this work, in order to demonstrate the capabilities of the new micromechanical technique, we analyze (70:30 wt%) poly (styrene-co-butyl acrylate) particles stabilized with poly (vinyl alcohol) at room temperature. They

are analyzed at room temperature rather than at typical film formation temperatures of the particles to prevent viscous behaviour in this initial investigation. The remainder of this work describes the materials, procedures, and results from this demonstration. Other system properties (i.e., temperatures, type of polymer, particle surface properties, etc.) and their effects on film formation were not analyzed here, but may be pursued in future research using the same techniques developed in this work. The potential of this new approach bodes great possibilities for understanding film formation mechanisms in water-borne coatings.

4. Materials and Methods

4.1 Forging of Microtools

There are two tools necessary for force measurements on dispersed polymer particles: the straight micropipette and the microcantilever. They must be forged in the laboratory prior to their application. Here, the necessary steps in their creation will be described.



Figure 11: Micropipette with closed end.

The first step in producing either a straight micropipette or a microcantilever is to create a tapered pipette with a closed end. A closed ended pipette is shown in figure 11. It is created using a machine called a pipette puller (David Kopf Instruments, Model 730) which uses a platinum iridium (Pt-Ir) wire to heat the middle section of a long glass tube (inner dia. 0.5mm, outer dia. 1mm) while pulling on its ends to elongate its centre until it is separated into two tapered pieces. What results from this pulling process are two drawn out micropipettes that are tapered down to closed ends and, depending on the heat applied through the platinum iridium wire, the length of the taper is suitable for either a microcantilever or a straight pipette. A longer taper, which is used for a microcantilever, is produced from a higher heat setting while a shorter taper, which is suitable for a straight pipette, is produced from lower heat settings.

Figure 12 shows a sketch of the pipette puller.

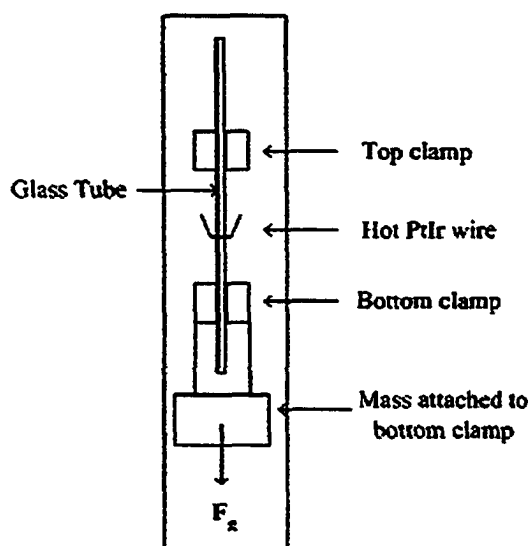


Figure 12: Pipette puller setup.

To be useful, the closed end of a micropipette must be truncated so that the opening can be exploited to apply suction pressures; typically, the inside diameter of the pipette end should be several micrometers. The procedure for truncating the tapered end of a pipette is carried out under a Zeiss Axiostar 100 microscope with a 10× objective. The closed ended micropipette is mounted on a micromanipulator capable of controlling the movement of the pipette in three directions. A platinum-iridium wire, with a small bead of molten glass suspended at its end, is mounted on a stand; it is heated by conducting an electrical current through it. The setup is shown in figure 14. As the glass bead on the wire melts, the closed ended pipette is extended into the molten glass. The required pipette end diameter is controlled by amount of insertion into the molten glass. When in position, the current through the platinum iridium wire is turned off, causing the pipette end and the glass bead (which is now firmly attached to the platinum wire) to solidify and fuse into one. Once fused, the micropipette end is broken off by pulling the pipette backwards. It is important to note that a smooth end on the

micropipette is required (i.e. not jagged). To make a smooth end, the same process is repeated again. This time, however, as the glass pipette is inserted into the molten glass bead, a small amount of liquid glass will flow up the open pipette (for about a distance of 10 microns) and remain there. When the electrical current through the platinum iridium wire is cut off, the molten glass inside the pipette solidifies and acts as a rigid internal support. As the pipettes pulls away from the glass bead and fractures, there will be a clean break around the rigid support, resulting in a micropipette with a smooth end which is perpendicular to the pipette axis . Figure 13 shows a truncated pipette, which can now be used as a tool for grasping and manipulating test samples. A straight pipette can further be shaped into a *microcantilever* for force measurement. The procedure for making a microcantilever is as follows:



Figure 13: Truncated micropipette.

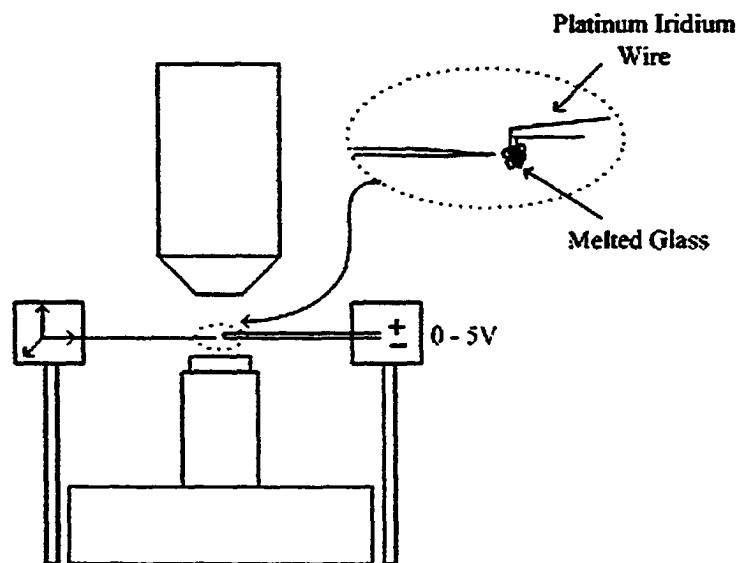


Figure 14: Pipette truncating setup.

A microcantilever is made by making two ninety degree bends in a long tapered micropipette, thus creating a “periscope” shape. Unlike in the previous case for the straight micropipette, a longer taper is necessary here so that two bends can be made before the tapered glass tube becomes too thick to bend. The technique to bend the glass involves using a platinum iridium wire as a forger to soften the glass. A setup similar to figure 14 is used here, except a thinner platinum iridium wire is used as the forger and an additional platinum iridium wire is mounted on a micromanipulator to act as a wire hook (for forcing the glass tube into a ninety-degree bend). The new setup is shown in figure 15. As shown in figure 16, there are now three objects in the microscope’s field of view: the cross section of a vertical platinum iridium wire, the glass pipette, and the additional hook-shaped wire for forcing the glass pipette into the desired configuration as it is heated. This system is used to make two bends in the glass tube that are in the same plane. The first bend in the glass is made close to the small open end, while the second bend is made at a chosen distance along the axis. The distance between the two bends is called the cantilever arm; depending on the desired cantilever stiffness, the cantilever arm may be made longer or shorter. (A longer cantilever arm has a lower spring constant, and vice versa.) The length of the cantilever arm can be anywhere from 0.5mm to 10mm. Once a cantilever is created, its profile (i.e., variation of radius along the arm) is measured so that the spring constant can be determined. The radius is measured using a scale on the eyepiece of the microscope. The theory for calculating the cantilever spring constant, along with a computer code, is given in Appendix A.

It is worth noting that the microtools produced using the above procedures are disposable. Disposability is important to ensure efficient execution of experiments: if a pipette breaks, it can be discarded and another one can be made again easily using the procedures above.

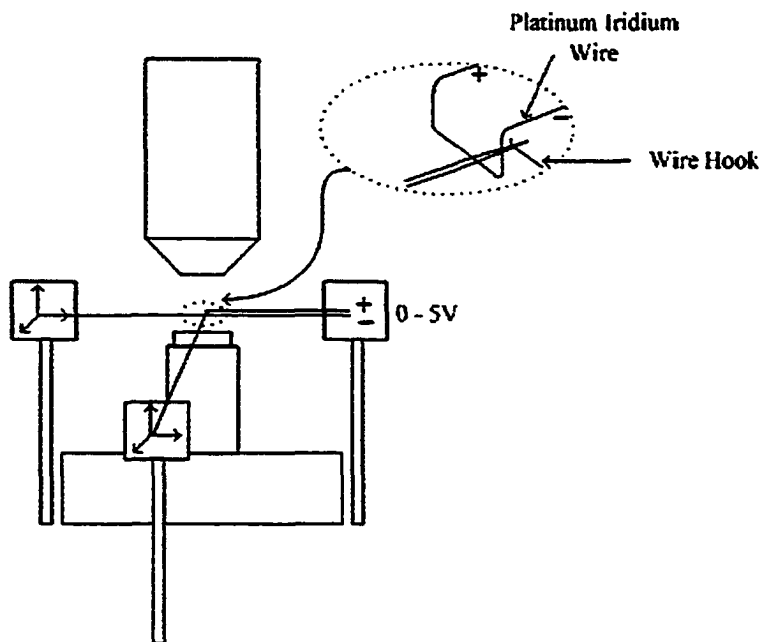


Figure 15: Setup for bending micropipettes into microcantilevers

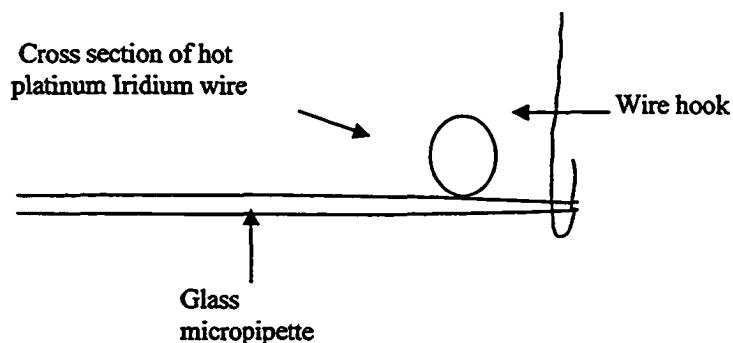


Figure 16: Setup for bending micropipettes into microcantilevers as seen under the microscope

4.2 Synthesis of Latex Particles

The latex particles used to demonstrate our micromechanical techniques were synthesized through suspension polymerization. This is a process whereby a

mixture of monomers, here styrene and butyl acrylate, is dispersed in water by mechanical agitation. The monomer droplets are polymerized while they are dispersed. This process results in particles that are larger than those produced in industrial emulsion polymerization systems since less surfactant is used. The following is a description of how the latex particles were synthesized for this work.

The initiator in the polymerization process was 2,2' azobis(2-methylpropionamide) dihydrochloride (V50) and was added at 0.5% (wt/wt on total monomers), 2% polyvinyl alcohol (PVA) (wt/wt on total monomers) was added as a dispersant.

The polymerization procedure was as follows: 6.547g styrene, 3.453g butyl acrylate, 0.2g PVA, and 0.05g V50 in 0.08mol/L aqueous solution, were added to 40 mL double distilled-deionized water. The mixture was bubbled with nitrogen for 30 minutes and was then applied to an ultrasonicator for 2 minutes. Reaction took place at 70°C for 4 hours and was stirred constantly at 600 rpm through the entire polymerization process. The resulting dispersed particles were then diluted to make them observable under a light microscope. Figure 17 shows a picture of the dispersed polymer particles of radius 5 to 20 μ m. Select particles were used from this dispersion to study film formation.

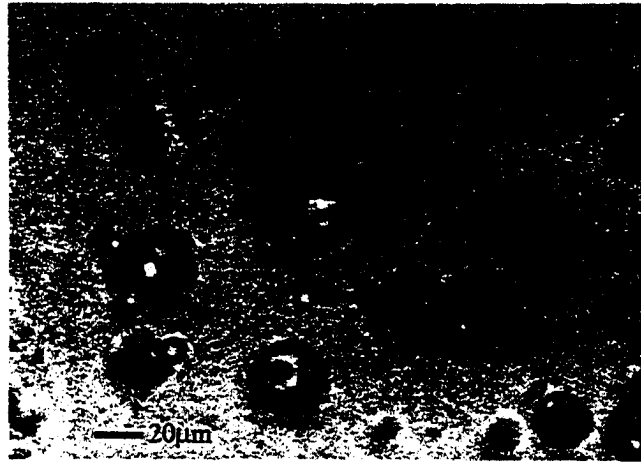


Figure 17: (70:30) Poly (styrene-co-butyl acrylate) latex dispersion stabilized with poly (vinyl-alcohol) as viewed under an optical microscope.

4.3 Glass Transition Temperature of the Latex Particles

Glass transition occurs when a polymer changes from a glass-like material to a rubber-like material (more precisely, to one which is viscoelastic) as the temperature is raised.¹⁵ The temperature at which this transition takes place is denoted T_g (the glass transition temperature). In this study, the T_g of the dispersed polymer particles was predicted using the known glass transition temperatures of both polystyrene (373K) and poly (butyl acrylate) (218K), and their relative ratios in the particles (70% and 30% respectively by weight). The approximate glass transition temperature was predicted to be 55°C using a weighted average:¹⁵

$$T_g = 0.3(218K) + 0.7(373K) = 327K \approx 55^\circ C \quad (17)$$

This value is consistent with a T_g of 48°C found by Sperry et al.¹⁴ for a (65:35 wt%) poly(styrene-co-butyl acrylate) latex dispersion. Knowledge of the approximate glass transition temperature helped in analysing the behaviour of the latex particles. Experiments were performed at room temperature, which is well

below the glass transition temperature of the particles. Latex dispersions typically do not form a film until they are close to their glass transition temperature. We therefore expected the polymer particles to be stiff, not easily deformed, and also unable to form a film.

4.4 Microscope Setup

The microscope used to view particle interactions was a Zeiss inverted microscope (Axiovert 200) with a 63× objective; it is set up on a vibration isolation table (Technical Manufacturing Corporation). Mounted on either side of the microscope were fine scale three-axis manipulators (Narishige) for microtool control. The image under the microscope was continuously recorded on a VCR and shown on a TV monitor. An “electronic callipers” device (Boeckeler Instruments, model VIA-100) was connected to measure both vertical and horizontal distances of microscopic images. In addition, a digital camera was used to take still pictures of objects under the microscope. Figure 18 shows the microscope setup.

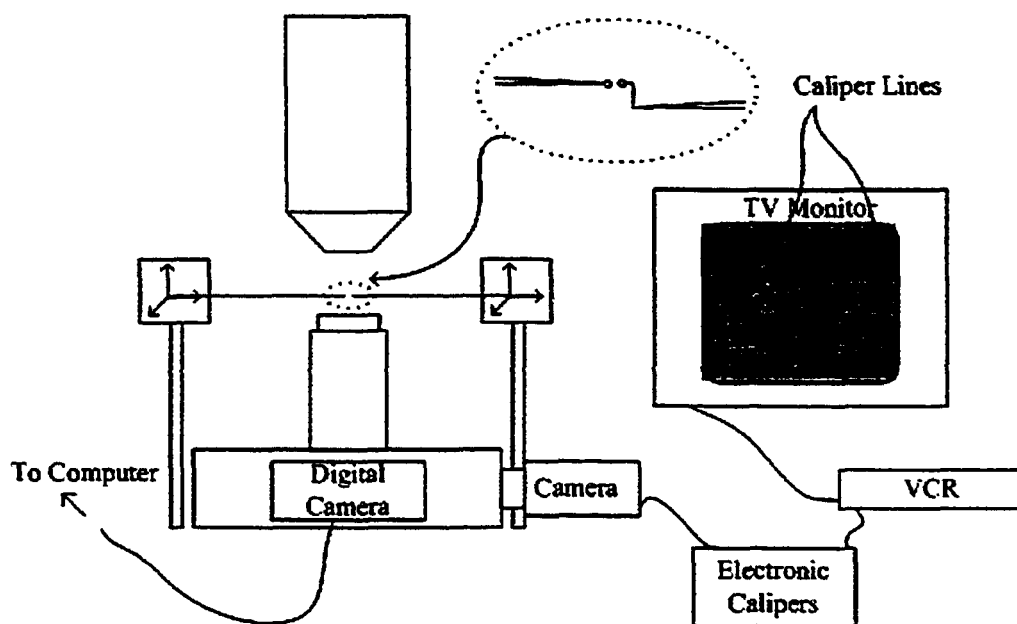


Figure 18: Microscope experimental setup

4.5 Isolating Individual Polymer Particles

To perform controlled experiments on two individual polymer particles, it was required to first isolate them from their original suspension. This was done every time a new particle was needed for testing in a clean environment — without the interference of other dispersed particles. The isolation process could be performed using either a straight micropipette or a microcantilever. The process used to extract particles was as follows: First, a drop of dilute dispersion was put on a hydrophobic slide. A hydrophobic slide was required so that the drop of latex dispersion would not spread on the glass. (The glass slide surface can easily be made hydrophobic through treatment of chemicals such as dichloro-dimethylsilane). Next, individual particles were left to settle on the slide and then observed with the microscope. At this point, a given microtool was chosen. The microtool was mounted on a manipulator and the suction pressure at the pipette's

open end was controlled by a syringe which is connected to the pipette via a tygon tubing. A small amount of water was first drawn into the pipette using suction pressure from the syringe. The reason for drawing water into the pipette was to create an aqueous environment inside the pipette prior to introducing it into the dispersion. The water-filled micropipette was then inserted into a suspension of polymer particles. Using the micromanipulators, the pipette tip was brought close to a selected particle — to within several micrometres. Next, with the suction pressure at the pipette tip activated (through negative pressure from the connected syringe), the particle can be picked up and held at the pipette end as shown in figure 19; the polymer particle shown had a diameter of 15 microns. The entire process was monitored in real time under an optical microscope.

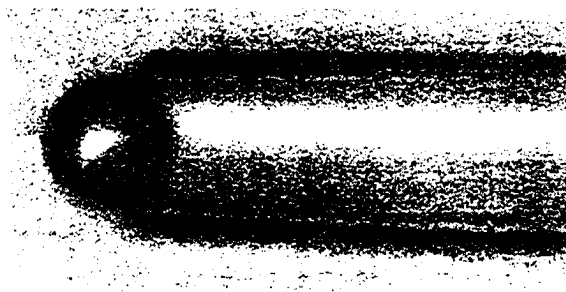


Figure 19: Particle on the end of a microtool.

Once firmly held by a microtool, the particle was removed from the dispersion by maintaining the suction with the syringe and moving the microtool and particle out of the dispersion. With a selected particle removed from the dispersion, its physical properties and interactions with other isolated particles could then be analyzed.

4.6 Tendency for Particle-Particle Adhesion

Before conducting experiments on the polymer particles at room temperature (i.e., below the glass transition temperature of the particles), a preliminary test was required to ensure that our larger polymer particles could indeed be used to demonstrate our micromechanical approach. Work of previous researchers had shown that larger particles typically required higher temperatures to coalesce.¹² Therefore, the large and high- T_g polymer particles used in this study were not expected to reach full coalescence. However, it was hoped that the larger particles would display the ability to at least adhere to one another. Once having demonstrated their ability to do so, further micromechanical studies could then be performed to determine the exact cause for such adhesion. To provide evidence for adhesion, a small quantity of latex dispersion was placed underneath a microscope and allowed to dry; the evaporation of the water and subsequent interaction between polymer particles was recorded in real time.

4.7 Elasticity of Individual Latex Particles

As the coalescence of latex particles must necessarily involve significant geometric deformations, the process will be opposed by the elasticity of the polymeric material. (Recall that experiments presented here are to occur at temperatures below T_g , suggesting that the particles are elastic in character.) Using micromechanical techniques which we have developed for this study, the *in situ* elastic modulus of individual latex particles was measured at room temperature to characterize their ability to resist coalescence. This was done,

quite simply, by pressing a polymer particle against a glass sphere and quantifying the resulting deformation. For analysis of this situation, the contact theory developed by Hertz²⁰ was utilized. Hertz's theory describes the elastic deformations of two solid spheres which are pressed together by an axial force. The theory is based on small strain deformation, with the elastic bodies exhibiting Hookean constitutive behaviours. The net compression of a sphere is given by

$$h = CF^{2/3} \quad (18)$$

where h is the deformation measure, F is the applied axial force, and C is a proportionality constant. Figure 21 illustrates the parameters h and F , indicating how the deformation of a polymer particle is measured in response to an applied force. In practice, the force F is detected by the microcantilever, while the deformation h is obtained from analysis of microscopic images.

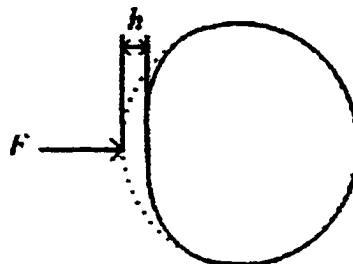


Figure 20: Solid spherical body deformed by an applied force.

To obtain the elastic modulus for a polymeric sphere, the relation of h vs. F must be obtained. With this relation, the proportionality constant C , which is a necessary value for calculating the elastic modulus, can be determined. The equation derived by Hertz to calculate the elastic modulus E of the polymer particle is:

$$E = \frac{3}{4} \frac{1-\nu^2}{C^{3/2} \sqrt{\frac{RR'}{R+R'}}} \quad (19)$$

where ν and R are, respectively, the Poisson's ratio and radius of the undeformed polymer particle, and R' is the radius of curvature of the glass sphere used to create deformation; the glass sphere is assumed rigid (i.e., its Young's modulus is assumed much larger than that of the polymer material, and therefore drops out of the problem).

As mentioned above, the compressive force F applied to the polymer particle was registered using a microcantilever. This cantilever was specially constructed such that a solid glass bead was melted onto its end as shown in figure 21a. For such an application, the bead could effectively be considered rigid (the Young's modulus of glass is typically 10^4 times that of rubber). This glass bead was used to push and deform a polymer particle. First, a single polymer particle (approx. $10 \mu\text{m}$ in diameter) was extracted from a dispersion with a straight pipette (see §4.5) and brought up to a microcantilever which has a glass bead attached to its end. The particle was then pushed against the glass bead in increments of several micrometres and the amount of particle deformation in each incrementation was measured. Figure 21b shows a close up of the experiment.

The displacements of the microcantilever corresponding to the particle deformations were measured using a video recording of a particular trial. Based on the known stiffness of the cantilever (see Appendix A for cantilever stiffness calculation), the force exerted on the polymer particle by the glass bead could be determined. Using this micromechanical technique, the h vs. F profiles for

individual polymer particles were obtained, thus allowing their elastic moduli E to be determined from equations (18) and (19).

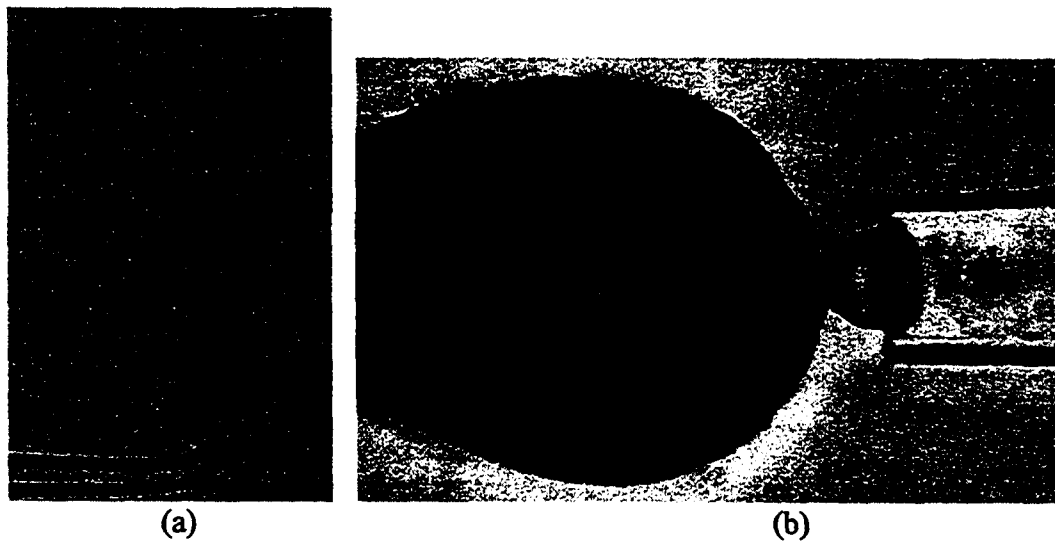


Figure 21: (a) A microcantilever with glass bead on its end. (b) Polymer particle (right) and glass bead (left) in the Hertz contact experiment. The polymer particle was about 10 microns in diameter; the glass bead on the left is a close-up of that in (a).

The above contact experiment was performed in both water and air to determine whether the particles were softened in an aqueous environment (the so-called *hydroplasticization* effect). Plasticization would be evident from a lowered elastic modulus in water. Several trials were completed in both air and water to obtain an average value for the elastic modulus in both situations.

4.8 The “Contact/Adhesion” Experiment

Because the polymer particles in this study were studied at temperatures below their glass transition (see §4.3), they were not expected to completely coalesce with each other as in the case for liquid drops. Nevertheless, two such particles may still adhere upon contact. Provided that adhesion does occur between

polymer particles, an important question arises: Does the strength of adhesion between two particles depend on the force of contact which brings them together? The answer to this question is provided by the “contact/adhesion” experiment (a name coined for this present study), which involves measuring the strength of *adhesion* between two particles after they are deliberately forced together under a given *contact force*.

The ability to determine how strong two particles adhere when forced together is crucial for understanding the roles of “*in situ* contact forces” in film formation. Here, “*in situ* contact forces” refers to the naturally occurring forces which act to pull the polymer particles together during film formation. Examples of such forces may be: capillary forces due to the air-water interfacial tension (§2.2), or the osmotic stresses which result from migration of water molecules across polymer layers (§2.4). In the contact/adhesion experiments, these *in situ* contact forces are replaced (i.e., mimicked) by externally applied forces through techniques of micromanipulation.

The contact/adhesion experiment was performed on two isolated latex particles: one held by a microcantilever and the other by a straight micropipette. A procedure of pushing the particles together with increasing contact forces, and pulling them apart to determine the resulting adhesive strengths, was carried out in both air and water environments. (In each case, the particles were allowed to remain in contact for one minute before separation.) The amount of compressive contact force was determined from the deflection of the cantilever to the left in figure 22, and the strength of adhesion was obtained from the maximum

cantilever deflection in the opposite direction (i.e., to the right in figure 22) as the particles were pulled apart.

It is important to note that, in an actual film formation process, the particles are not pushed together and separated multiple times. The repeated tearing of the particle surfaces as they are pulled apart is likely to cause unwanted changes to the surface properties. To minimize this effect, a particular pair of particles were pushed together and pulled apart for no more than two times. Following two adhesive tears, two new particles were isolated from the dispersion and used in the experiment. Particles of comparable size were used. In the course of performing these contact/adhesion experiments, cantilevers of different elastic stiffnesses were used. Different cantilever stiffnesses were required to accommodate the different ranges of forces.



Figure 22: Two polymer particles being pushed together in a “contact/adhesion” experiment.

4.9 Simulating Water Evaporation

In their natural environments, polymer spheres may coalesce and form film coatings under the influence of various driving forces. Some of the driving forces behind film formation have already been discussed in Chapter 2 (Literature Review), where different theories on the mechanism(s) of film formation have

been reviewed. Figure 23 illustrates some of the proposed mechanisms which may induce — or prevent — film formation:

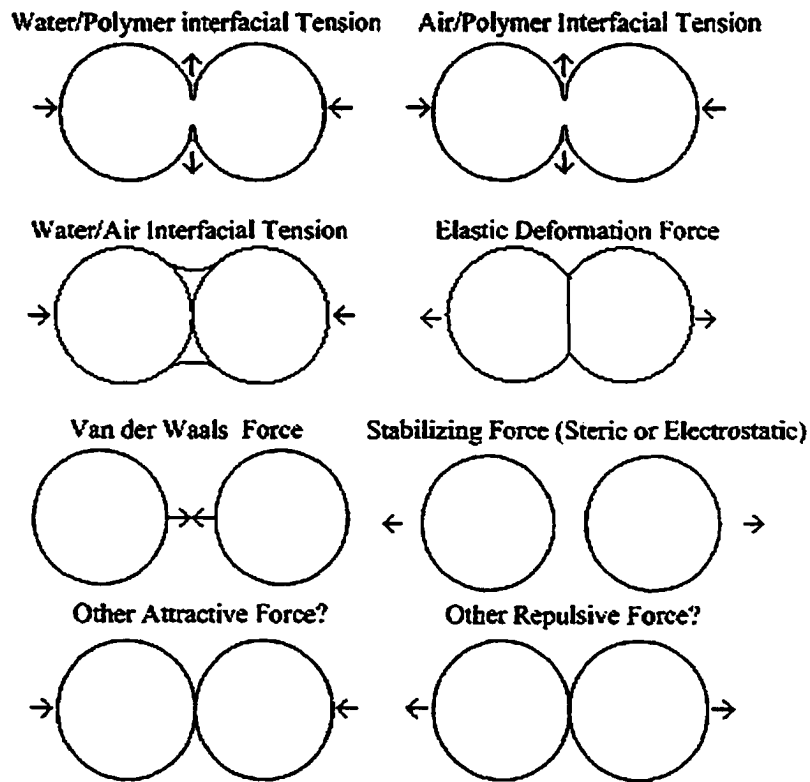


Figure 23: Naturally occurring forces which may be responsible for film formation.

The question of whether water/polymer interfacial tension or air/polymer interfacial tension plays a role in particle-particle adhesion (corresponding to, respectively, wet and dry sintering) will be addressed in the contact/adhesion experiments (see §4.8), where polymer spheres are manipulated into contact in air and in water. In this section, we propose a method of studying the effect of the water/air interfacial tension on adhesion. This is done by artificially recreating the condition of water evaporation around two polymer spheres. It is well known that, as the water evaporates, the surface tension of water will give rise to forces which pull the particles together; these forces are often referred to as capillary

forces. Here, we wish to determine if capillary effects are strong enough to trigger adhesion between particles. The experiment proceeds as follows: Using techniques of micromanipulation, two polymer particles are isolated from a suspension. One particle is attached to a straight micropipette, while the other is held by a microcantilever; the spheres are initially in gentle contact. A third pipette, which is filled with water, is then brought close to the particles near their contact point. A small amount of water is expelled from the water-filled pipette, creating a liquid bridge between the two particles as shown in figure 24. Due to the small scale of this experiment (approx. $10\ \mu\text{m}$), the water bridge will evaporate completely in only several seconds. Any adhesion between the two particles after water evaporation can be registered by the microcantilever.

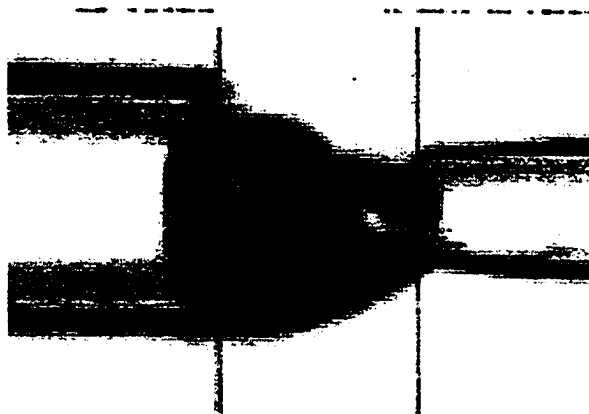


Figure 24: Water bridge between two polymer spheres. The larger particle (on the left) is roughly $18\ \mu\text{m}$ in diameter. The water as shown evaporated within seconds.

5 Results and Discussion

5.1 Tendency for Particle-Particle Adhesion

Before conducting quantitative experiments on the latex particles, a visualization test was first performed at room temperature (see §4.6). The purpose of this preliminary experiment was to check for the potential of the latex particles to adhere to one another. This type of experiment can serve as a “screening test” if one were to examine a number of different polymer types. The experiment involves, quite simply, observation of water evaporation under a microscope, and to look for signs of particle-particle adhesion at the end of the drying process. Figure 25a shows the initial suspension of polymer spheres in water; only one drop (approx. 30 μL) of this suspension was deposited onto the glass slide. After approximately 20 minutes, the water evaporated completely, leaving clusters of polymer spheres as shown in figure 25b. (Because the particle concentration in figure 25a was deliberately made dilute, only small clusters of particles resulted.)

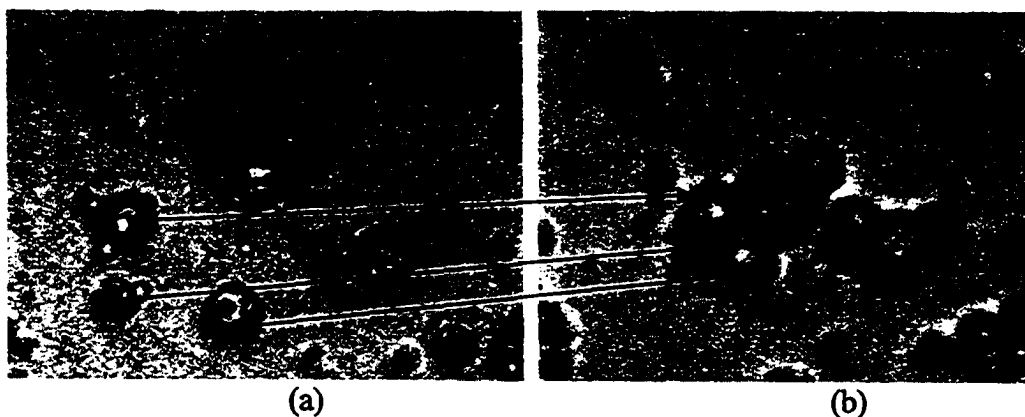


Figure 25: (a) A dispersion of poly(styrene-co-butyl acrylate) spheres in water. (b) After evaporation of the surrounding water, the particles are seen to have bonded. Individual particles are tracked by the arrows.

As seen in figure 25b, there is strong evidence that the particles had adhered to one another. This result prompted further analysis to determine what caused such

adhesion. In addition to observing the end result of particle-particle adhesion from this experiment, the real-time kinetics of the process were also observed. While in suspension, the polymer particles remained dispersed and uncoalesced. But as water evaporated around the particles, they were drawn together by the water surface tension and eventually bonded to one another. The transformation between figures 25a and 25b occurred within 5 seconds.

There is no question that capillary effects (i.e., forces resulting from the air-water interfacial tension) are responsible for drawing suspended particles together as the water evaporates. What remains unanswered at this point is: Do capillary effects also play a role in the adhesion of polymer spheres? Or do they simply bring the particles into close contact so that other colloidal forces can become important? To determine which effects are responsible for the adhesion shown in figure 25b, the interactions between the polymer spheres must be studied closer. This is where the ability to examine interactions between individual particles in simulated environments (with special microtools) is extremely useful.

5.2 Elasticity of Individual Latex Particles

As seen in the previous section, at room temperature (i.e., below the glass transition temperature of $\sim 55^{\circ}\text{C}$), the latex particles were not able to completely coalesce upon water evaporation. The resistance to complete coalescence was almost certainly due to the elasticity of the polymer material. Here, the elastic moduli of individual polymer spheres will be characterized in their in situ

environments. (This is in contrast to traditional methods in the literature, which only quantify the elasticity of dried films.) As discussed in section 4.7, the elastic modulus of the latex spheres could be directly measured using novel micromechanical techniques. The experiment was based on Hertz's classic analysis of contact between two elastic spheres.²⁰ Here, experimental data from the Hertz contact experiment (i.e., h and F) were obtained using a straight micropipette (which captured single polymer spheres) and a microcantilever (with a glass bead at its end); the procedures were described in §4.7. From the h vs. F data, the proportionality constant C was found by linearizing Hertz's relation (eqn 18) as follows:

$$\log h = \frac{2}{3} \log F + \log C \quad (20)$$

To obtain the value of C , $\log h$ vs. $\log F$ data was plotted and the y-intercept of a best fit line, with slope $2/3$, was used to calculate C using the relationship:

$$C = e^{\text{y-intercept}} \quad (21)$$

To check for effects of hydroplasticization (i.e., softening of the polymer by water), the Hertz contact experiment was conducted both in air and in water. The data from four trials are given in Appendix B (Tables 2 to 5). Tables 2 and 3 are from the Hertz experiments done in air, and Tables 4 and 5 are from experiments done in water. Figures 26 and 27 below show, respectively, the linearized data $\log h$ vs. $\log F$. Figures 26 through 27 therefore represent one set of data from experiments done in air and one from experiments done in water. The remaining graphs associated with Tables 3 to 5 are given in Appendix B.

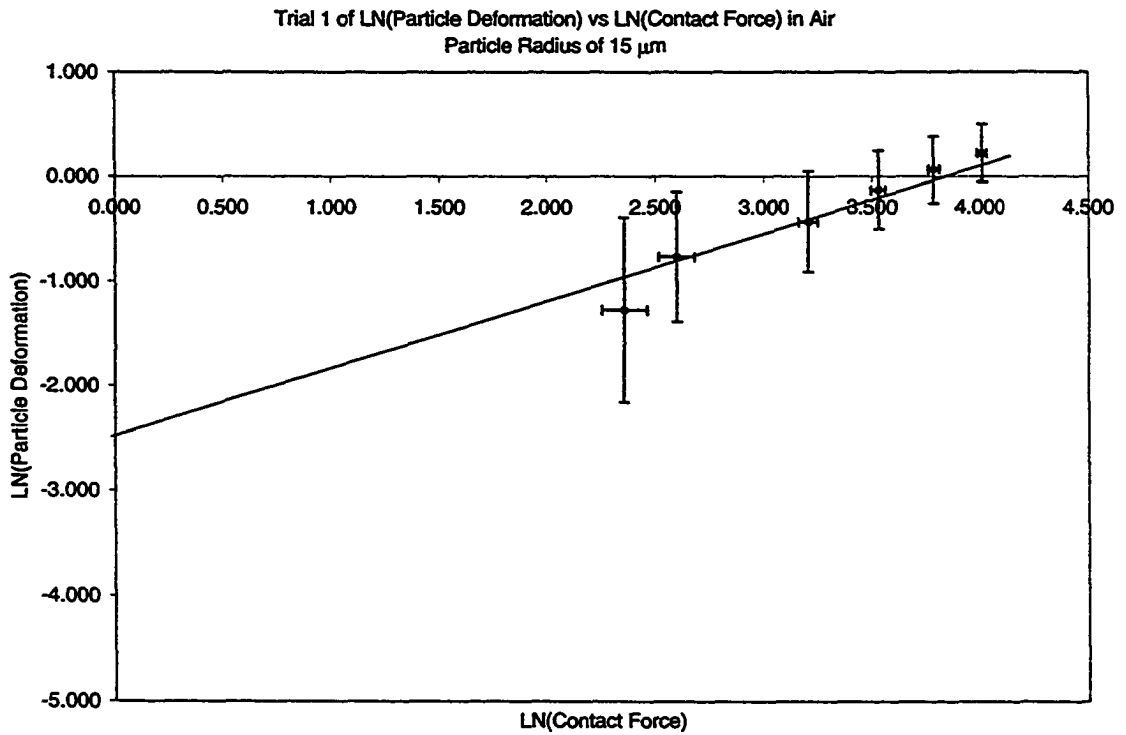


Figure 26: Trial 1 of $\log h$ vs. $\log F$ in air (particle radius = 15 μm).

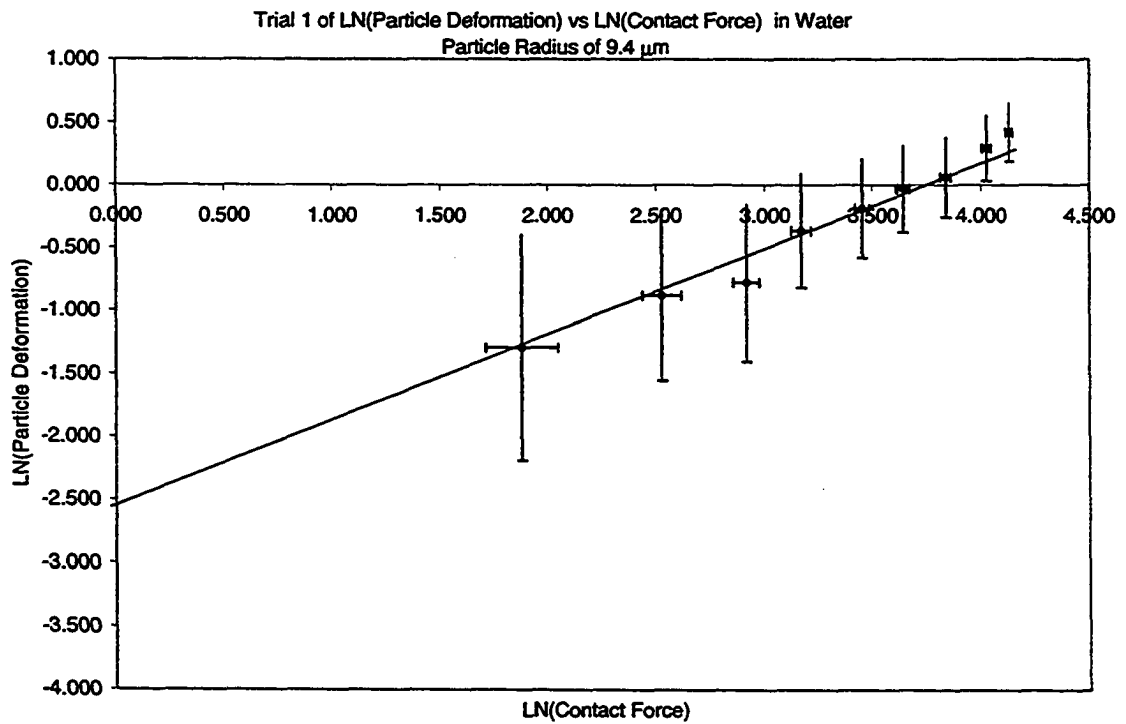


Figure 27: Trial 1 of $\log h$ vs. $\log F$ in water (particle radius = 9.4 μm).

The least squares fits in figures 26 and 27 both yielded a common y-intercept of -2.5. (One should not be concerned with the units of this y-intercept, as logarithms are taken to obtain power relationships.) This y-intercept was used to calculate the proportionality constant C as follows:

$$\text{y-intercept} \approx -2.5 \quad (22)$$

$$C = \exp(-2.5) \approx 0.08 \mu\text{m}/(\mu\text{N})^{2/3} \quad (23)$$

Figures 26 and 27 represent measurements of the elastic moduli in, respectively, air and water. Since both plots resulted in a common proportionality constant C (which can in turn be directly related to the polymer elastic constant; see eqn (19), we arrive immediately at an important conclusion: for the copolymer (70:30 wt%) poly (styrene-co-butyl acrylate), there was no evidence of hydroplasticization at room temperature.

Knowing the value of C , one can estimate the elastic modulus of the polymer as follows: Defining R as the radius of the polymer sphere, R' as the radius of the rigid glass bead, and using $\nu \approx 0.4$ for the Poisson's ratio²⁴ of an incompressible substance, we have

$$R \approx 10 \mu\text{m} \quad (24)$$

$$R' \approx 30 \mu\text{m} \quad (25)$$

$$\nu \approx 0.4 \quad (26)$$

$$E = \frac{3}{4} \frac{1-\nu^2}{C^{3/2} \sqrt{\frac{RR'}{R+R'}}} \approx 10 \text{ MPa} \quad (27)$$

In using equation 27 (or eqn 19), it was assumed that the glass bead was much more rigid than the polymer sphere; as a result, the elastic modulus of the glass

bead did not enter into the analysis. This assumption can now be verified *a posteriori*: the Young's modulus of the polymer in question is estimated to be 10 MPa (eqn 27), while that of glass is typically 7×10^4 MPa.

For the latex used in this study, the estimated elastic modulus of 10 MPa is comparable to the elasticity of dried films below their glass transition temperature, but is high in comparison to films close to or above their glass transition temperature²⁵. Such a high value was expected for our particles since, at room temperature, they are well below their glass transition temperature (§4.3). With a large elastic modulus, one would expect the coalescence of the latex particles to be greatly inhibited. This is confirmed through the observation that our particles are only able to adhere and not coalesce (§5.1). This, however, is not a negative finding, as the particles are still able to adhere under the influence of natural forces (despite large elastic resistance). This suggests that the same natural forces which pull the latex spheres together will have a much bigger effect on softer particles — when the operating temperature is closer to the glass transition, and the elastic modulus is much lower.

5.3 The Contact/Adhesion Experiment

The contact/adhesion experiment, as described in section 4.8, was carried out with the assumption that pushing two particles together would cause them to adhere, and that the amount of adhesion would increase with the contact force that is being exerted. From such experiments, we wish to find the approximate relationship between particle adhesion and contact force. The experiment was

carried out at room temperature in both air and water, with particles approximately 10 μm in diameter.

Contact/adhesion in air

In air, it was found that the particles did adhere as suspected. The plot in figure 28 shows an increasing adhesive force as the force of contact became stronger. (Recall that the force of contact was directly measurable from the deflection of the cantilever, while the force of adhesion was determined from the maximum recoil of the cantilever as the particles were pulled apart; see §4.8.) The data in figure 28 comprised of all of the data from eight trials done with four pairs of polymer spheres. Each pair of particles was pushed together and pulled apart only twice. The raw data from the contact/adhesion experimental trials are shown in Table 6 in Appendix B.

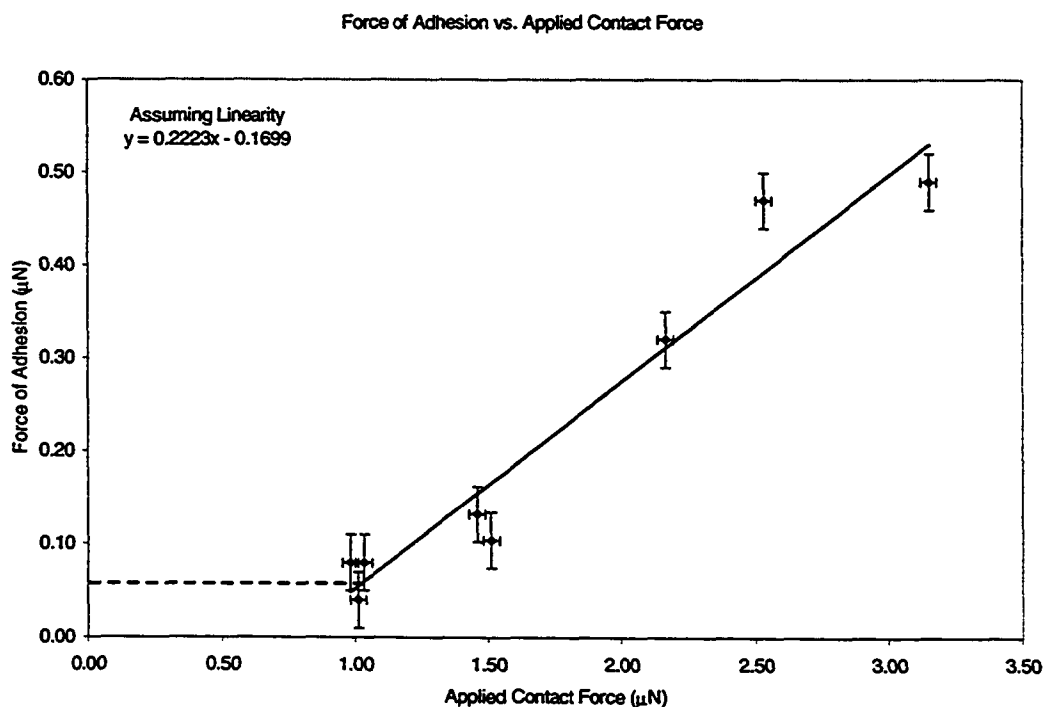


Figure 28: Direct measurements of the force of contact (the applied force) vs. the force of adhesion (the resulting “sticking force”) between two polymer spheres in air.

The horizontal dotted line in figure 28 represents all contact forces that were 1 μN or less (to a point where they were undetectable by the cantilever). In all these cases, it was observed that a finite attraction between the spheres was present — due simply to the fact that the spheres were in physical contact. As seen in the figure, the level of this adhesion was constant at about 0.05 μN . It is interesting to note that this attraction persisted even as the surfaces of the particles were sheared past one another. This strongly suggests that the adhesion was not due to dry sintering (driven by the air/polymer interfacial tension), as the shearing action would disrupt any such bonding. We believe this weak attraction is likely due to van der Waals interaction. In what follows, we will refer to this baseline adhesive force of 0.05 μN (the dotted line in figure 30) as “van der Waals attraction” — although we acknowledge that the origin of this force is, at this point, not yet conclusive.

For contact forces larger than 1 μN , the data in figure 30 exhibits a roughly linear relationship. Within this range, a linear regression was made between the forces of adhesion and the forces of contact; the result is

$$\text{Contact Force} \approx \frac{\text{Adhesion Force} + 0.17}{0.22} \quad (28)$$

where both the Adhesion Force and the Contact Force have units of μN , and the former is larger than 0.05 μN . This relationship can be used to obtain approximate magnitudes for natural contact forces that cause measurable particle adhesion. For example, if a certain natural force causes adhesion of two particles

(with magnitude $> 0.05 \mu\text{N}$), the above linear equation can be used to find the approximate value of the natural contact force that caused such an adhesion.

Contact/adhesion in water

In addition to conducting contact/adhesion experiments in air, the same tests were also performed in water. In this case, the adhesion between two polymer spheres was undetectable even when subjected to much larger contact forces (compared to those applied in air). Here, the maximum applied contact force was approximately $10\mu\text{N}$, which is four to five times larger than their counterparts in air (figure 30). This information is very valuable: The lack of adhesion in water indicates that the stabilizing forces due to the polymer dispersant are very efficient in keeping the particles dispersed in aqueous suspension. Even when brought into contact and pushed together, they would not adhere. From this result, we conclude that, unless the latex particles are partially coalesced before being submerged in water, they will likely not destabilize as a latex suspension (which can be very undesirable in coatings applications).

5.4 Simulating Water Evaporation

Based on the results of contact/adhesion experiments in the previous section, it was clear that latex particles in aqueous suspension are not likely to adhere. Yet, the polymer spheres do adhere when a latex suspension is spread onto a substrate and the water is allowed to evaporate (see figure 25). The adhesion must therefore be triggered by the drying process, perhaps as a result of capillary forces pulling the polymer spheres together. To investigate this capillary effect, the

interaction between two latex particles was examined as water evaporated around them. The procedure for this experiment was described in section 4.9.

In the experiment, two polymer spheres were manipulated into gentle contact and a small amount of water is deposited onto the assembly (figure 24). After the water evaporates (which took only several seconds on the micron scale), the particles were pulled apart. As we learned from the results in the previous section (figure 30 in particular), for two latex particles that are just touching in an air medium, the adhesive force is expected to be around $0.05 \mu\text{N}$. However, the measured adhesion force, based on experiments on three pairs of particles, averaged at around $0.5 \mu\text{N}$ — an order of magnitude larger than expected! (To minimize disruption to the surface structure, water was allowed to evaporate only twice around each pair of particles.) The adhesion data are given in Table 7 in Appendix B.

Based on an adhesion force of $0.5 \mu\text{N}$, one can use the linear regression from the previous section (equation 28) to predict the corresponding contact force:

$$\text{Contact Force} = \frac{\text{Adhesive Force} + 0.17}{0.22} = \frac{0.5 + 0.17}{0.22} \approx 3 \mu\text{N} \quad (29)$$

For the given level of adhesion ($0.5 \mu\text{N}$), the two polymer spheres apparently had to be pushed together by a contact force of $\sim 3 \mu\text{N}$; this force stems presumably from capillary effects. It is possible to predict such a force, theoretically, in the simple case when two rigid spheres (of equal size) are connected by a liquid bridge. In the limit when the volume of the liquid is much smaller than that of the

spheres, the capillary force which draws the spheres together is independent of the liquid volume. This force is given by the simple relation²⁶

$$F_{\text{contact}} = 2\pi R \gamma \quad (30)$$

where R is the radius of the spheres and γ is the interfacial tension between the liquid and the surrounding medium. Typically, for $R = 10\mu\text{m}$ and with an air/water interfacial tension of $\gamma = 73 \text{ mN/m}$, the contact force is estimated to be $\sim 4.5 \mu\text{N}$. This is very close to the contact force inferred from the contact/adhesion experiments ($3\mu\text{N}$) and may in fact correspond further if one takes into consideration a lowered water/air interfacial tension due to the presence of surfactant molecules (dispersants) in the water. Such agreement lends support to the notion that capillary forces which result from water evaporation are responsible for the adhesion of polymer spheres.

Following water evaporation, we further tested an additional environment assuming that air/polymer interfacial tension might cause additional polymer adhesion because of a larger contact area. However, this was not the case. After waiting for 10 minutes, it was clear that the strength of adhesion did not exceed the level attained immediately after water evaporation. The reason for this is likely because of the stiff nature of the latex particles. Additional adhesion may have presented itself if the particles were softer.

For the two forces which caused adhesion of the latex particles (van der Waals and capillary effects), real time video was collected to show the measurement process. Such video is a very valuable visual tool to demonstrate the effects that the natural forces have on the particles.

5.5 Mechanism of Particle-Particle Adhesion

Based on our experimental results, we may now suggest a mechanism for how the latex particles bonded together in our preliminary particle-particle adhesion test.

We know that in their initial water environment, the dispersed particles were not able to adhere. This is confirmed from our contact/adhesion experiment in water, where two particles were put in intimate contact in a water environment. We observed that even when the particles were pushed together with significant forces they would not adhere. This result suggests heavily that no *in situ* force could possibly be responsible for causing the particles to bond while they were submerged in water.

Similar to a submerged water environment, a dry environment was also insufficient to cause adhesion of our particles. From the contact/adhesion experiment in air, we found that large contact forces were required to generate significant adhesion between two particles. Only small “van der Waals” type attractions were detectable between the particles when they were simply brought into contact. This result suggest that clusters of dry particles could not possibly bond to one another on their own.

The fact that our latex particles could not have bonded in a water or an air environment implies that bonding must have occurred solely through capillary forces due to the evaporation of water. Experimental evidence supports this claim. In our preliminary particle-particle adhesion test, realtime observations revealed that the evaporation of water appeared to draw the particles together. These observations rose our suspicions that water evaporation (capillary force) was

the main contributor causing a bond between the particles. Our suspicions were confirmed when the simulation of water evaporation between two particles caused significant adhesion between them.

From this result, which identifies the importance of water evaporation, it is interesting to highlight that in a number of experiments carried out by past researchers (i.e. Sheetz, Mahr, Dobler, Sperry, and Lin and Meir); the dispersions were first dried well below their glass transition temperature before experiments were performed on them. It was assumed by these researchers that by drying the particles well below their glass transition they would remain uncoalesced because of their rigid nature. Following drying, these “uncoalesced” films were often used to demonstrate that coalescence could occur by wet sintering or dry sintering alone, without water evaporation. The results from this work suggests that in those experiments, the particles may have in fact broken stabilization barriers after initial drying. If this were true, then the polymer particles were already well connected thus permitting coalescence in environments where coalescence may have never otherwise occurred.

5.6 Future Work

In this work, we have limited ourselves to a specific case study to investigate the potential of our micromechanical techniques, further research may therefore be conducted at higher temperatures and with different types of polymer particles to determine whether film formation occurs by different mechanisms in different case studies. Since full coalesce is possible, but not observed here, we can expect

that differences would arise in response to different system parameters. Many questions still need answering to gain a deeper understanding of film formation. The micromechanical techniques described in this case study possess great potential for answering these many questions.

6 Conclusions

The subject of film formation is very complicated. The main concern in this area over the years has been the question of the main driving forces causing film formation. What causes the particles to pack together and what drives the coalescence process? Using a new micromechanical approach, we hope to unravel a lot of the questions still unanswered in this area. What makes this new approach so valuable is that it involves studying larger particles that are observable under a light microscope and easily manipulated with special microtools. The process is therefore very visual and because interactions between individual particles can be studied, information about the basic unit of film formation (two particle coalescence) is obtainable. With information about the basic unit, generalizations can be made about an entire film forming system.

A demonstration of the micromechanical technique is presented using (70:30) poly (styrene-co-butyl acrylate) particles stabilized with poly (vinyl alcohol). Experiments were conducted on these particles to understand their behaviour in response to different colloidal forces in typical film formation environments. All experiments were performed at room temperature, a temperature significantly below the T_g of the polymer of interest. Using a Hertz contact experiment these particles were found to be very stiff with an elastic modulus of approximately 10 MPa. A high modulus was expected for the particles because of a predicted glass transition temperature of 55°C. The large modulus and was not a negative finding since a preliminary test proved that the particles still exhibited an ability to adhere. Their ability to adhere despite their

high elastic modulus implied that the forces responsible for adhesion would have a much larger impact if the particles were less stiff.

First observations of the drying process from our preliminary particle-particle adhesion test, lead us to believe that water/air interfacial tension from water evaporation was the main contributor to the adhesion of our particles. However, we were not absolutely certain. To obtain a closer look at the types of natural forces that were responsible, we employed our special microtools.

To analyze the forces responsible for causing adhesion of our polymer particles, different *in situ* environments where questionable natural forces would flourish were simulated. We found that capillary force from water evaporation between the particles was the only *in situ* force able to cause them to adhere, allowing us to conclude that water/air interfacial tension was the sole force causing a bond between our latex particles, while stabilizing forces and the high elastic modulus of our particles worked to prevent them from coalescing.

The most important result of this work was that we were able to demonstrate the effectiveness of our micromechanical technique for determination of forces influential in causing the attraction and adhesion of particles in a given film formation system. Since we have only studied one particular type of polymer system at room temperature, it is important to note that additional research may be conducted to look further into the effect of other system parameters on film formation. Therefore, we have essentially broken the ground for more research using our micromechanical technique.

Bibliography

1. A. F. Routh and W. B. Russel, *Ind. Eng. Chem. Res.*, 40, (2001), 4302
2. T.W. Wirth and P. Pfoehler, *Surface Coatings Australia*, 33, (1996), 14
3. V. Verkholtantsev, *Europ. Coatings J.*, 1, (1998), 60
4. R.E. Dillon, L.A. Matheson and E.B. Bradford, *J. Colloid Sci.*, 6, (1951), 108
5. G. L. Brown, *J. Polym. Sci.*, 22, (1956), 423
6. J.W. Vanderhoff, H.L. Tarkowski, M.C. Jenkins, and E.B. Bradford, *J. Macromolec. Chem.*, 1, (1966), 361
7. D.P. Sheetz, *J. Appl. Polym. Sci.*, 9, (1965), 3759
8. T.G. Mahr, *J. Phys. Chem.*, 74, (1969), 2160
9. G. Mason, *Br. Polym. J.*, 5, (1973), 101
10. J. Lamprecht, *Colloid Polym. Sci.*, 258, (1980), 960
11. K. Kendall and J.C. Padget, *Int. J. Adhes. Adhes.*, 2, (1982), 149
12. S.T. Eckersley and A. Rudin, *J. Coat. Technol.*, 62, (1990), 89
13. F. Dobler, T. Pith, M. Lambla, and Y. Holl, *J. Colloid Interface Sci.*, 152, (1992), 1-21
14. P. R. Sperry, B.S. Snyder, M.L. O'Dowd, and P.M. Lesko, *Langmuir*, 10, (1994), 2619
15. R.J. Young and P.A. Lovell, *Introduction to Polymers 2nd ed.*, Chapman and Hall (1991)
16. J.L. Keddie, P. Meredith, R.A.L. Jones, and A.M. Donald, *Macromolecules*, 28, (1995), 2673
17. F. Lin and D.J. Meier, *Langmuir*, 11, (1995), 2726
18. P.A. Steward, J. Hearn, M.C. Wilkinson, *Adv. Colloid Interface Sci.*, 86, (2000), 195
19. J. Frenkel, *J. Phys. (Moscow)*, 9 (1943), 385

20. L.D. Landau and E.M. Lifshitz, *Theory of Elasticity*, Pergamon, Oxford, (1970).
21. W.H. Yang, *J. Appl. Mech. (Trans. ASME)*, (1966), 395
22. K.L. Johnson, K. Kendall, and A.D. Roberts, *Proc. R. Soc. London, Ser.A*,324, (1971), 301
23. K. Moran, A. Yeung, and J. Masliyah, *Langmuir*, 15, (1999), 8497
24. J.Brandrup and E.H. Immergut, *Polymer Handbook 3rd ed.*, John Wiley and Sons (1989)
25. M.P.J. Heuts, R.A. le Febre, J.L.M. van Hilst, and G.C. Overbeek, Ch.18, ACS Symposium Series 648, *Film Formation in Waterborne Coatings*.
26. R.J. Hunter, *Foundations of Colloid Science, Vol. I*, Clarendon Press, Oxford (1986).

Appendix A

Calculation of Cantilever Spring Constant

By calculating how a cantilever theoretically responds to forces, we can calculate its theoretical spring constant. Beam theory is used to calculate theoretical horizontal displacements dh for applied horizontal forces F_h . Figure 29a shows the beams in a given cantilever and figure 29b shows the forces on a cantilever as well as the deflection of a cantilever in response to those forces.

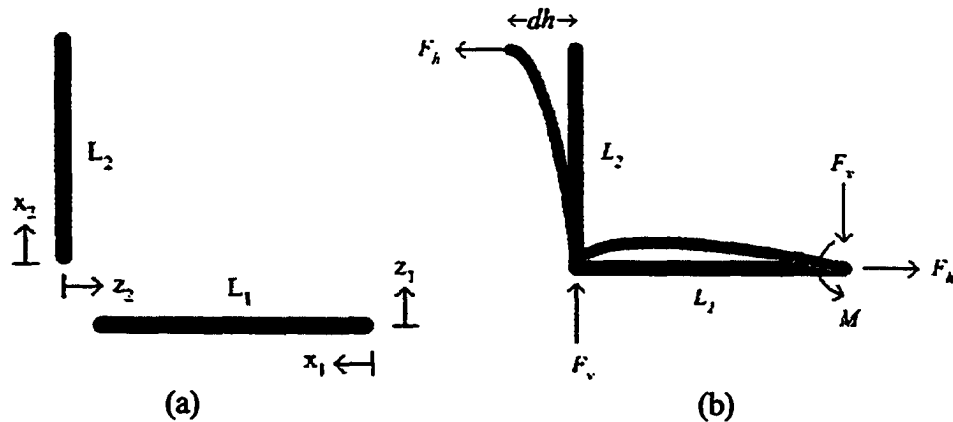


Figure 29: (a) Individual Beams of a cantilever. (b) Forces on cantilever.

A typical beam obeys a differential equation describing how it bends in response to force.

$$\frac{d^2 z_i(x_i)}{dx_i^2} = \frac{M_i(x_i)}{E_g I_i(x_i)} \quad (31)$$

where $z_i(x_i)$ is the deflection of a beam, E_g is the beam material's elastic modulus, $I_i(x_i)$ is the beams moment of inertia, $M_i(x_i)$ is the bending moment, and i signifies the beam or member under discussion (i.e. beam 1 or beam 2 in the cantilever).

Using the radial geometry of the beam, the moment of inertia can be calculated:

$$I_i(x_i) = \frac{\pi}{4} (r_{out_i}(x_i))^4 \left(1 - \left(\frac{r_{in_i}(x_i)}{r_{out_i}(x_i)} \right)^4 \right) \quad (32)$$

where $r_{ini}(x_i)$ and $r_{out}(x_i)$ are the inner and outer radius of the microcantilever along its length. The ratio of the two is approximately 0.6. We obtain the radial geometry by measuring it under a microscope when the cantilever is created.

The bending moments along the beams in the microcantilever are found by moment

balances:

$$M_1(x_1) = F_v L_1 \left(1 - \frac{x_1}{L_1}\right) - F_h L_2 \quad (33)$$

$$M_2(x_2) = -F_h L_2 \left(1 - \frac{x_2}{L_2}\right) \quad (34)$$

where L_1 and L_2 are the lengths of the beams in the cantilever, and F_v and F_h are the vertical and horizontal forces on the cantilever.

Equation (28) must be solved for both beams in the cantilever simultaneously.

This is done by reducing the equation to two first order ODEs as follows:

$$y_{2i}(x_i) = z_i(x_i) \quad (35)$$

$$y_{1i}(x_i) = \frac{dz_i(x_i)}{dx_i} \quad (36)$$

$$\frac{dy_{1i}}{dx_i} = \frac{M_i(x_i)}{E_g I_i(x_i)} \quad (37)$$

$$\frac{dy_{2i}}{dx_i} = y_{1i} \quad (38)$$

These ODEs are solved with numerical methods using physical boundary conditions:

$$y_{1i}(0) = 0 \quad (39)$$

$$y_{2i}(0) = 0 \quad (40)$$

$$dv = -y_{2i}(\text{at cantilever elbow}) = 0 \quad (41)$$

where the boundary conditions in (36) and (37) state that the beam is rigid at the cantilever elbow and at the beginning of the first beam ($x_1 = 0$ and $x_2 = 0$) and therefore the displacements and rates of change in displacement at those points are approximately zero. The boundary condition in (38) states that the vertical displacement at the elbow of the cantilever dv is zero. This can be achieved in an actual experiment by supporting the cantilever elbow.

After solving the two simultaneous ODEs, horizontal displacement comes out of the result of the beam deflections.

$$dh = -[y_{21}(\text{at cantilever neck}) + L_{12}(\text{at cantilever elbow})] \quad (42)$$

The second term in horizontal displacement is due to the rotation of the cantilever about the cantilever elbow. Values of horizontal displacements dh can be calculated for a set of horizontal forces F_h to obtain the spring constant for a given cantilever.

Matlab Numerical Analysis

What follows is an example input and output for calculating the spring constant of a cantilever

```

INPUT
%*****
%SYMBOL DEFINITIONS
%x_1 - distances along horizontal beam starting opposite cantilever elbow.
%r_1 - outer radius of glass pipette associated with x_1
%x_2 - distance along vertical beam starting at cantilever elbow.
%r_2 - outer radius of glass pipette associated with x_2
%L1 - length of cantilever beam 1
%L2 - length of cantilever beam 2

```

```

%phi - ratio of inner radius of glass pipette to outer radius (approximately 0.6)
%E - elastic modulus of glass (approximately 70,000 MPa)
%x1 - variable distance along horizontal beam starting opposite cantilever elbow
%x2 - variable distance along vertical beam starting a cantilever elbow
%Fh - horizontal force
%Fv - vertical force
%Fvl - left bound guess of vertical force
%Fvr - right bound guess of vertical force
%dv - vertical displacement
%dhg - horizontal displacement to graph
%Fhg - horizontal force to graph
%z1 - beam 1 deflection
%dz1 - first derivative of beam 1 deflection
%z2 - beam 2 deflection
%dz2 - first derivative of beam 2 deflection
%*****
%OBTAIN GEOMETRY AND PROPERTIES OF MICROCANTILEVER.
fprintf('Input geometry of microcantilever.')
fprintf('You will now enter the outer diameter values you have measured along
each beam \n')
fprintf('Put distances and associated diameter in two row vectors enclosed by
square brackets\n')
fprintf('x_i should have the same number of elements as d_i \n')
%
x_1 = input('Enter row vector of x_1 values in millimeters:');
%x_1 = [0 1 2 3 4 5 6];
d_1 = input('Enter row vector of d_1 values in scale on small microscope:');
%d_1 = [21 17 14 12 11 11 12];
x_2 = input('Enter row vector of x_2 values in millimeters:');
%x_2 = [0 1 2 3 4 5];
d_2 = input('Enter row vector of d_2 values in scale on small microscope:');
%d_2 = [12 12 12 11 10 6];
%Convert input units to micrometers and convert diameters to radii
x_1 = x_1*1000;
x_2 = x_2*1000;
r_1 = d_1*1000/460;
r_2 = d_2*1000/460;
%Use arrays to determine length of beams.
L1 = x_1(length(x_1));
L2 = x_2(length(x_2));
%Elastic Modulus
E = 70000;
%Inner to outer glass ratio
phi = 0.6;
%*****

```

%HORIZONTAL DISPLACEMENT FOR CORRESPONDING HORIZONTAL FORCE

%Set up loop for finding horizontal displacements hd for different horizontal forces.

%Set up an inner loop to find associated appropriate vertical forces that will cause the vertical displacement to be zero. First enter high and low guess for vertical

%force.

%Fvl = input('Enter low bound guess for vertical force in micro-newtons: ');

%Fvr = input('Enter high bound guess for vertical force in micro-newtons:');

for i = 1

Fvl = 0;

Fvr = 10;

dv = 1;

Fh = i/2;

while dv ~= 0

Fv = 1/2*(Fvr+Fvl);

%Export an array of constants into a file that can be imported into %functions. This is required because differential equation functions do %not allow anymore than two arguments.

save variables Fh Fv L1 L2 E phi x_1 x_2 r_1 r_2;

%Solve the two second order differential equations

%Specify initial conditions

initial_1 = [0; 0];

initial_2 = [0; 0];

[x1,num_y1] = ode45(@eqns2_1,[0 L1],initial_1);

[x2,num_y2] = ode45(@eqns2_2,[0 L2],initial_2);

%Define vertical displacement with current Fv and Fh

z1 = num_y1(:,2);

dv = -z1(length(z1));

%Criterion for small vertical displacement

if abs(dv) < .00000001

dv = 0;

end

%Create new right bound if Fv guess is on right side of answer

if dv < 0

Fvr = Fv;

end

%Create new left bound if Fv guess is on left side of answer

if dv > 0

Fvl = Fv;

end

%dv

end

z1 = num_y1(:,2);

z2 = num_y2(:,2);

```

dz1 = num_y1(:,1);
dz2 = num_y2(:,1);
dhg(i) = -(z2(length(z2))+L2*dz1(length(dz1)));
Fhg(i) = Fh;
end
subplot(2,2,1),plot(x1,z1),xlabel('x1'),ylabel('z1')
subplot(2,2,2),plot(x2,z2),xlabel('x2'),ylabel('z2')
format long
spring_const = Fhg(1)/dhg(1)
Fhg(2) = 0;
dhg(2) = 0;
subplot(2,2,3),plot(dhg,Fhg),xlabel('dh'),ylabel('Fh')

```

END INPUT

The following functions are matlab files and are called in the ODE calculations above. They are called eqns2_1.m and eqns2_2.m and should be placed in the same file folder as the above program.

```

function y1_prime = eqns2_1(x1,y1)
load variables;
a(1) = (Fv*L1*(1-x1/L1)-Fh*L2)/(E*(pi/4*(1-phi)^4)*(interp1(x_1,r_1,x1,'spline'))^4);
a(2) = y1(1);
y1_prime = a';

function y2_prime = eqns2_2(x2,y2)
load variables;
a(1) = -Fh*L2*(1-x2/L2)/(E*(pi/4*(1-phi)^4)*(interp1(x_2,r_2,x2,'spline'))^4);
a(2) = y2(1);
y2_prime = a';

```

OUTPUT

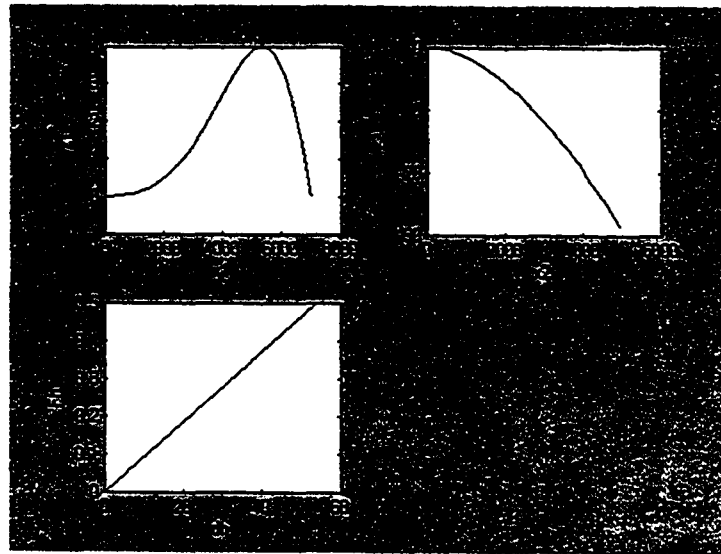


Figure 30: Deflections of Beams (Displacements in Micrometers and Forces in MicroNewtons)

spring_const = 0.00924254420104 N/m

Appendix B

Hertz Contact Experiment

Force (μN) (± 1.1)	Deformation of Particle (μm) (± 0.2)	LN(Force)	LN(Deformation)	LN(Force) error	LN(Deformation) error
0.0	0.0	-	-	-	-
10.6	0.3	2.357	-1.273	0.104	0.887
13.4	0.5	2.597	-0.766	0.082	0.621
24.6	0.7	3.204	-0.431	0.045	0.480
34.1	0.9	3.529	-0.128	0.032	0.375
44.0	1.1	3.784	0.063	0.025	0.319
55.0	1.3	4.007	0.223	0.020	0.278

Table 2: Trial 1 of Hertz experiment in air (particle radius = $15\mu\text{m}$)

Force (μN) (± 1.1)	Deformation of Particle (μm) (± 0.2)	LN(Force)	LN(Deformation)	LN(Force) error	LN(Deformation) error
0.0	0.0	-	-	-	-
11.7	0.4	2.456	-0.994	0.094	0.733
25.3	0.7	3.231	-0.301	0.043	0.432
37.0	1.0	3.610	-0.025	0.030	0.344
50.4	1.2	3.920	0.148	0.022	0.296
63.4	1.4	4.149	0.329	0.017	0.253
76.3	1.5	4.335	0.422	0.014	0.233
92.2	1.9	4.524	0.615	0.012	0.196
108.5	2.1	4.686	0.732	0.010	0.176
118.6	2.3	4.776	0.839	0.009	0.159

Table 3: Trial 2 of Hertz experiment in air (particle radius = $9\mu\text{m}$)

Force (μN) (± 1.1)	Deformation of Drop (μm) (± 0.2)	LN(Force)	LN(Deformation)	LN(Force) error	LN(Deformation) error
0.0	0.0	-	-	-	-
6.5	0.2	1.878	-1.687	0.168	1.151
11.0	0.3	2.398	-1.124	0.100	0.802
19.0	0.4	2.946	-0.994	0.058	0.733
22.6	0.5	3.118	-0.673	0.049	0.579
29.7	0.6	3.392	-0.589	0.037	0.543
39.2	0.8	3.670	-0.242	0.028	0.412
45.2	1.0	3.811	0.015	0.024	0.332
54.7	1.2	4.002	0.182	0.020	0.288
61.8	1.3	4.125	0.259	0.018	0.269

Table 4: Trial 3 of Hertz experiment in water (particle radius = $9.4\mu\text{m}$)

Force (μN) (± 1.1)	Deformation of Drop (μm) (± 0.2)	LN(Force)	LN(Deformation)	LN(Force) error	LN(Deformation) error
0.0	0.0	-	-	-	-
6.5	0.3	1.878	-1.291	0.168	0.898
12.5	0.4	2.525	-0.879	0.088	0.675
18.4	0.5	2.914	-0.777	0.060	0.626
23.8	0.7	3.169	-0.364	0.046	0.455
31.5	0.8	3.450	-0.186	0.035	0.393
38.1	1.0	3.639	-0.030	0.029	0.345
46.4	1.1	3.837	0.063	0.024	0.319
55.9	1.3	4.023	0.293	0.020	0.261
62.4	1.5	4.134	0.422	0.018	0.233

Table 5: Trial 4 of Hertz experiment in water (particle radius = $9.4\mu\text{m}$)

Trial 1 of Particle Deformation vs. Contact Force in Air
Particle Radius of 15 μ m

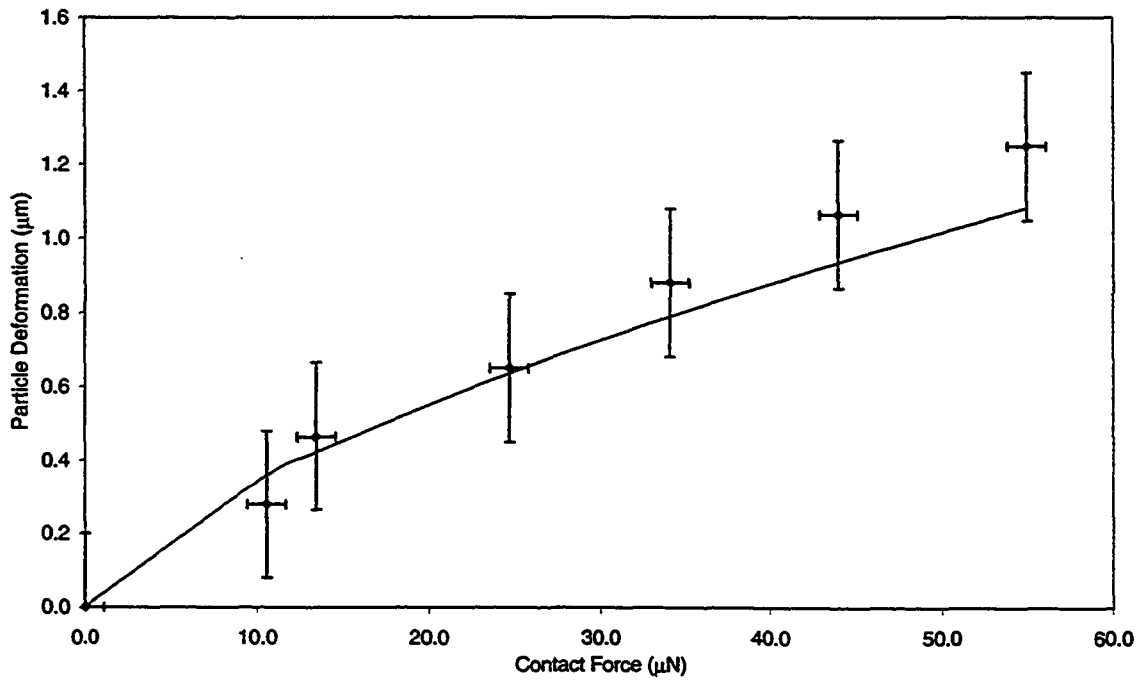


Figure 31: Trial 1 of particle $\ln(\text{deformation})$ vs. $\ln(\text{contact force})$ in air
(particle radius = 15 μ m)

Trial 1 of LN(Particle Deformation) vs LN(Contact Force) in Air
Particle Radius of 15 μ m

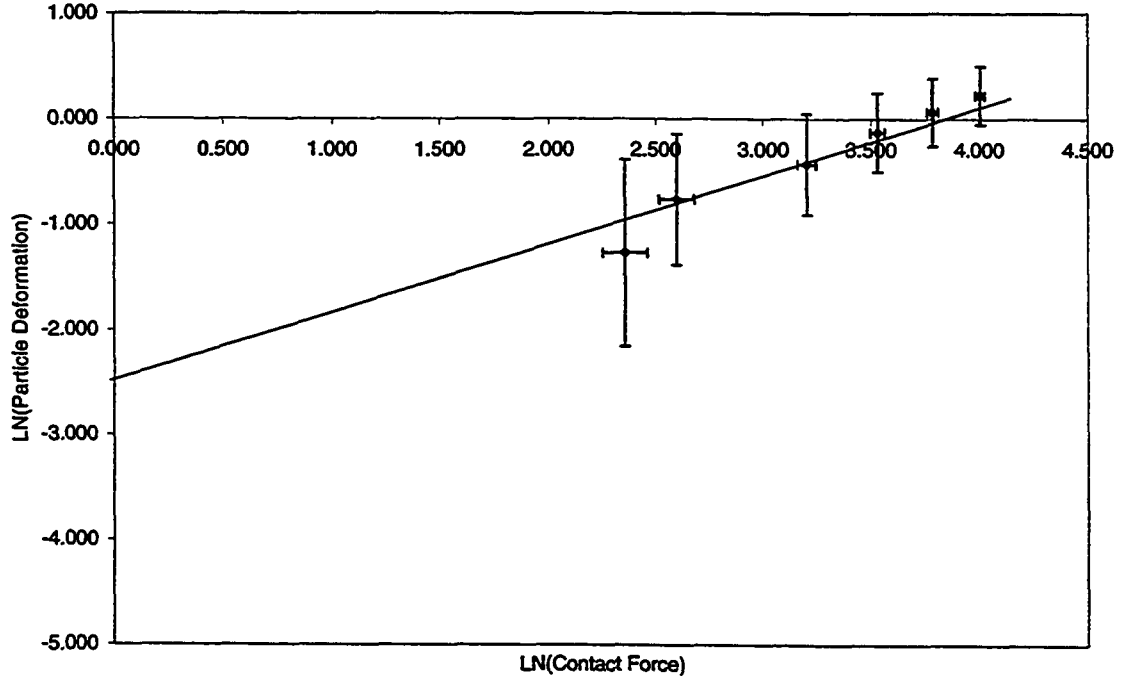


Figure 32: Trial 1 of particle deformation vs. contact force in air
(particle radius = 15 μ m)

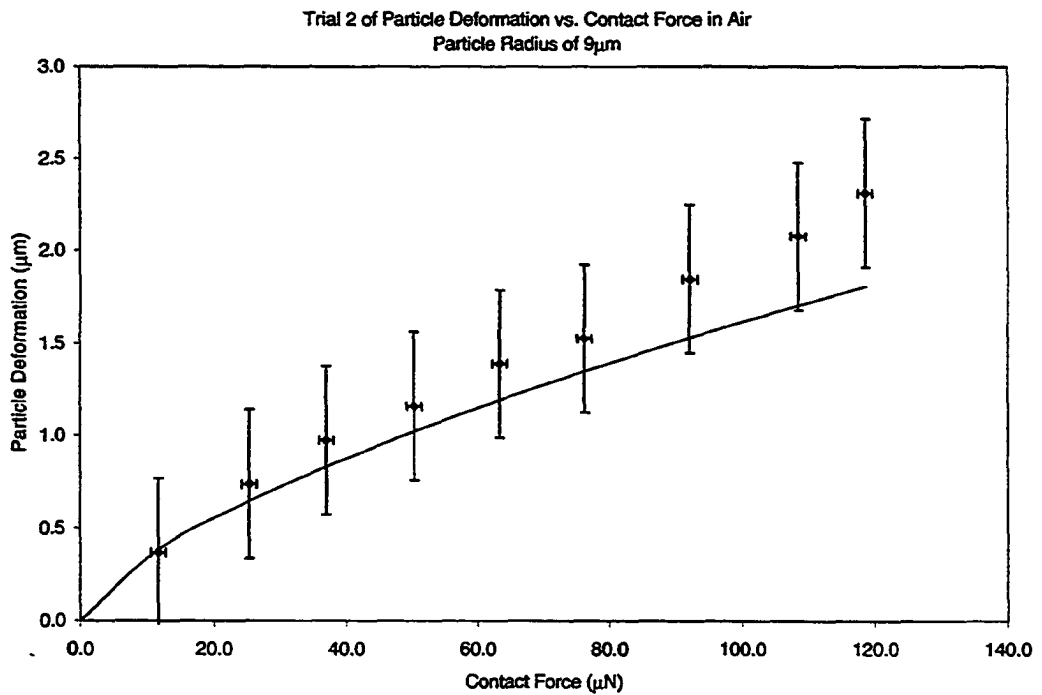


Figure 33: Trial 2 of particle deformation vs. contact force in air
(particle radius = $9\mu\text{m}$)

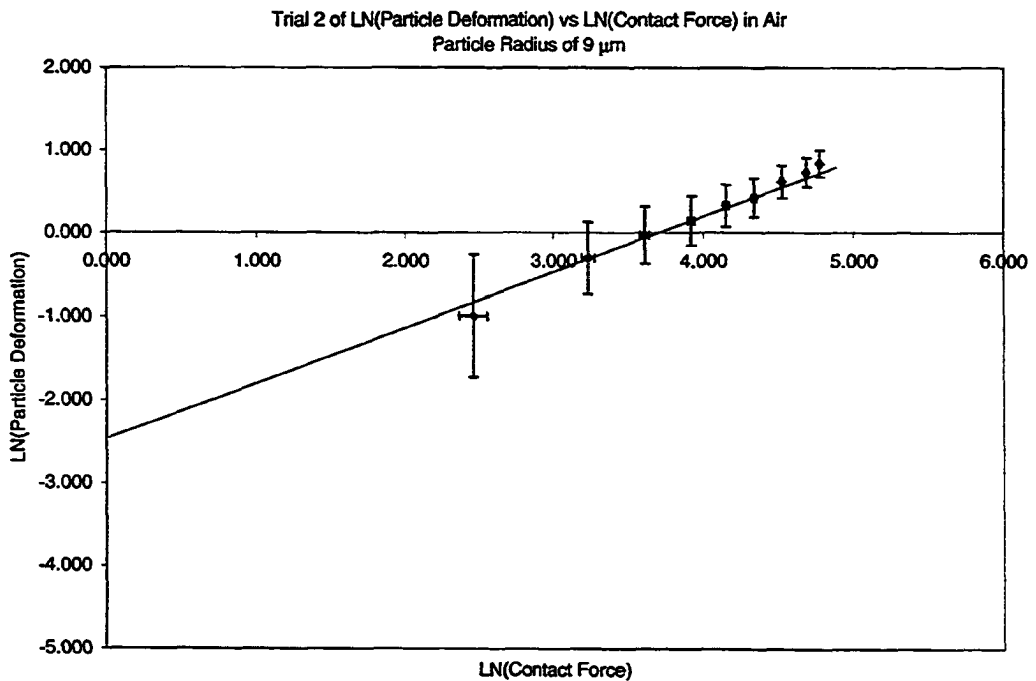


Figure 34: Trial 2 of particle $\ln(\text{deformation})$ vs. $\ln(\text{contact force})$ in air
(particle radius = $9\mu\text{m}$)

Trial 1 of Particle Deformation vs. Contact Force in Water
Particle Radius of $9.4\mu\text{m}$

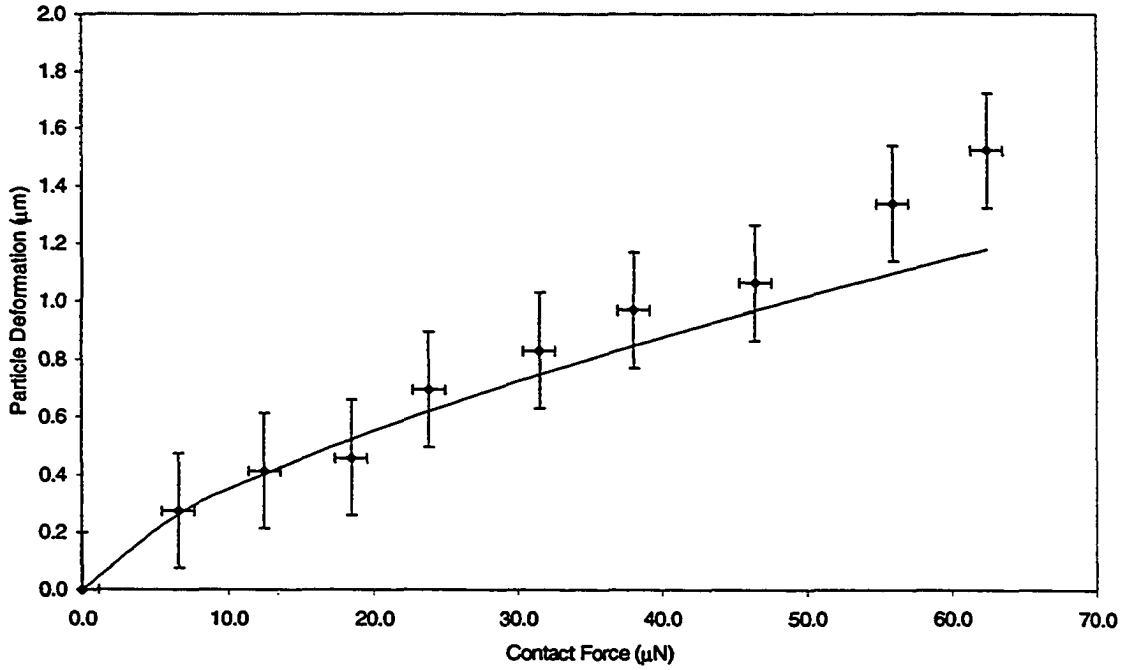


Figure 35: Trial 1 of particle deformation vs. contact force in water
(particle radius = $9.4\mu\text{m}$)

Trial 1 of LN(Particle Deformation) vs LN(Contact Force) in Water
Particle Radius of $9.4\mu\text{m}$

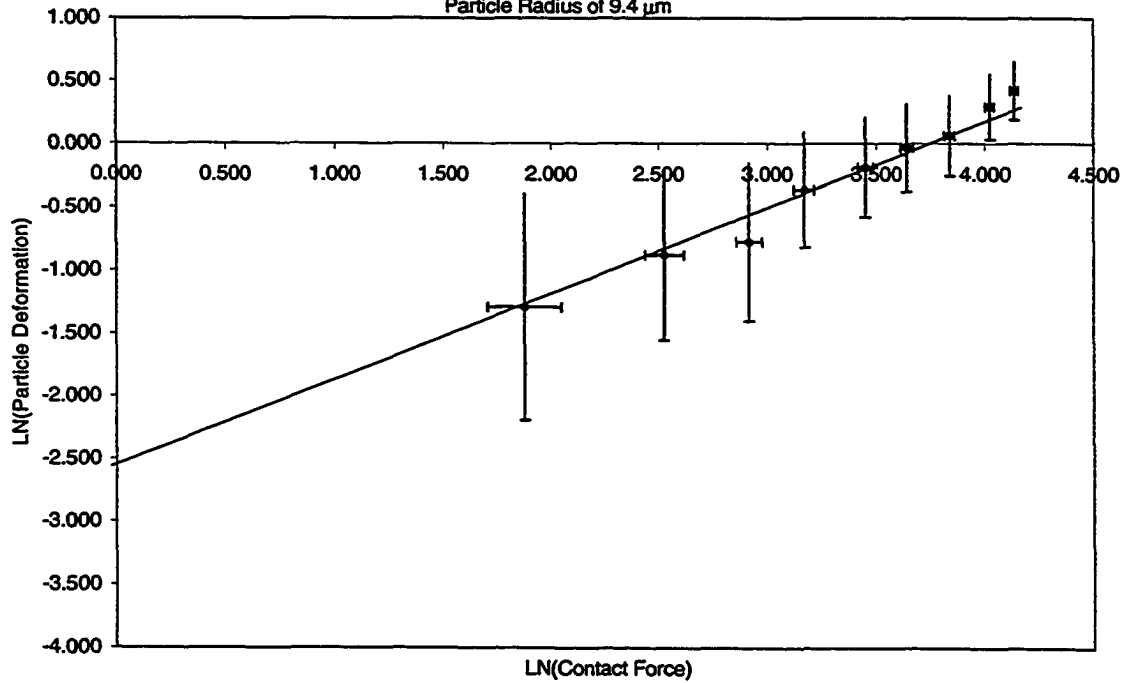


Figure 36: Trial 1 of particle $\ln(\text{deformation})$ vs. $\ln(\text{contact force})$ in water
(particle radius = $9.4\mu\text{m}$)

Trial 2 of Particle Deformation vs. Contact Force in Water
Particle Radius of $9.4\mu\text{m}$

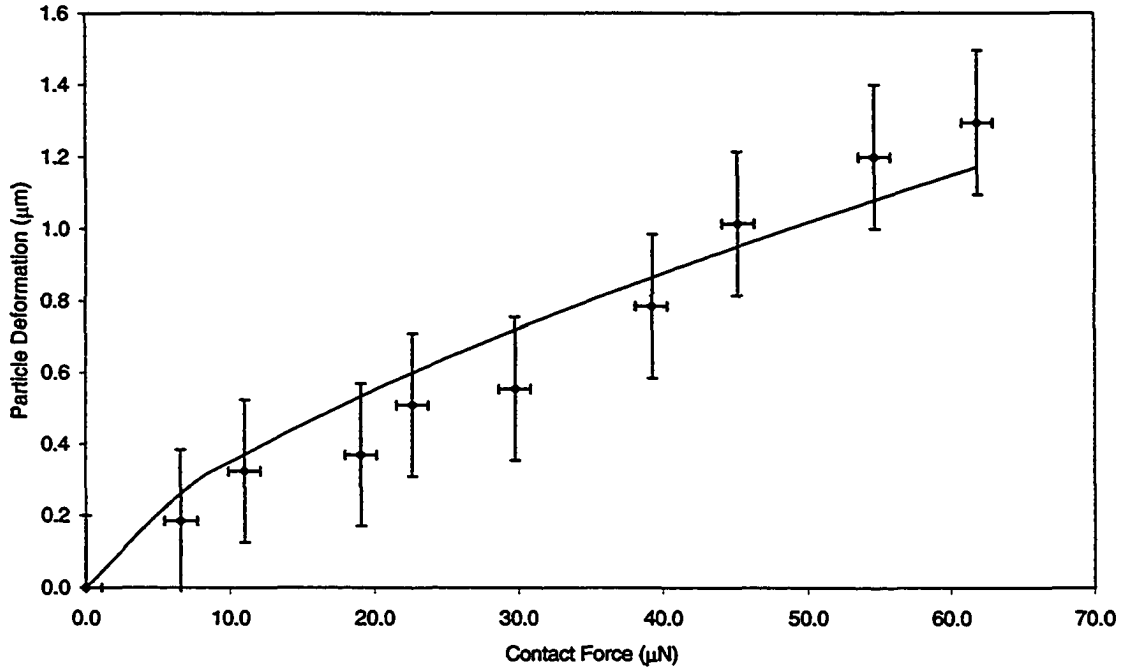


Figure 37: Trial 2 of particle deformation vs. contact force in water
(particle radius = $9.4\mu\text{m}$)

Trial 2 of LN(Particle Deformation) vs LN(Contact Force) in Water
Particle Radius of $9.4\mu\text{m}$

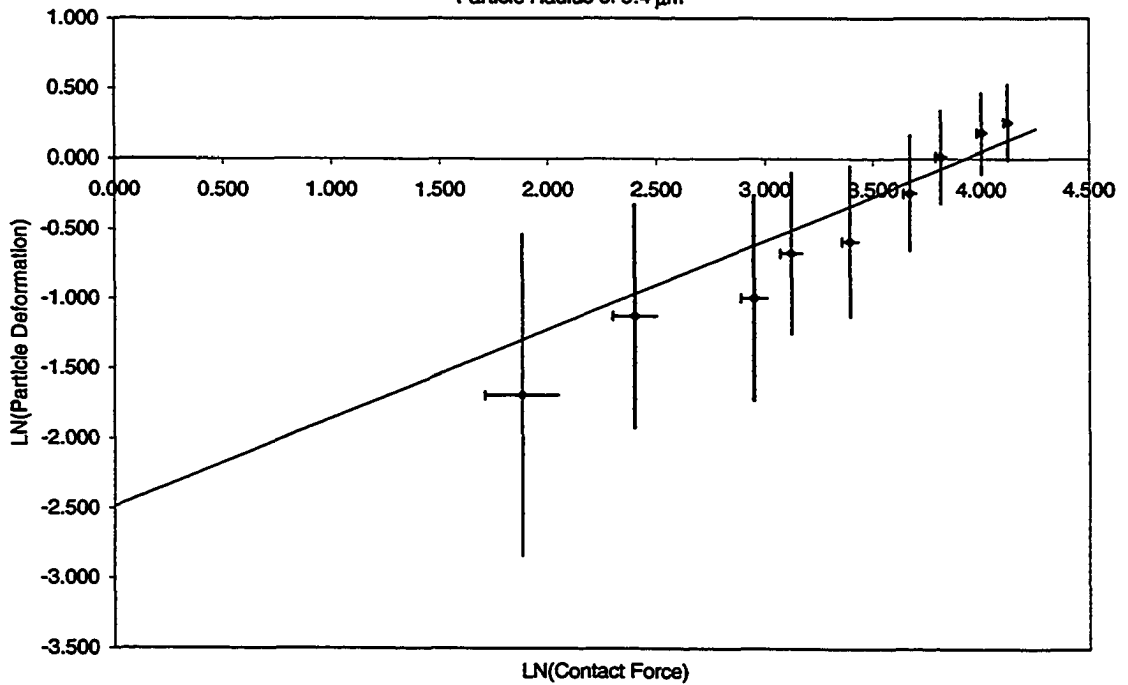


Figure 38: Trial 2 of particle $\ln(\text{deformation})$ vs. $\ln(\text{contact force})$ in water
(particle radius = $9.4\mu\text{m}$)

Contact/Adhesion Experiment

Particle Set	Force to Push Particles Together (μN) (± 0.03)	Resulting Adhesive Force (μN) (± 0.03)
1	2.53	0.47
	3.15	0.49
2	1.03	0.08
	1.01	0.04
3	1.46	0.13
	0.98	0.08
4	2.16	0.32
	1.51	0.10

Table 6: Trials for contact/adhesion experiment (particle radii = $10\mu\text{m}$)

Adhesion from Water Evaporation

Particle Set	Force of Adhesion (μN)
1	0.71
	0.46
2	0.42
	0.62
3	0.41
	0.33
Average	0.49

Table 7: Trials for adhesion due to capillary attraction (particle radii = $10\mu\text{m}$)